Forschungszentrum Jülich
in der Helmholtz-Gemeinschaft

Institut für Schichten und Grenzflächen
Institut 1: Halbleiterschichten und -bauelemente
Abteilung Ionentechnik

Fabrication and characterization of ultra-fast Si-based detectors for near infrared wavelenghts

Dan Mihai Buca

Jül-4075

Fabrication and characterization of ultra-fast Si-based detectors for near infrared wavelenghts

Dan Mihai Buca

Berichte des Forschungszentrums Jülich ; 4075
ISSN 0944-2952
Institut für Schichten und Grenzflächen
Institut 1: Halbleiterschichten und -bauelemente
Abteilung Ionentechnik Jül-4075
D38 (Diss., Köln, Univ., 2002)

Zu beziehen durch: Forschungszentrum Jülich GmbH · Zentralbibliothek
D-52425 Jülich · Bundesrepublik Deutschland
☎ 02461/61-5220 · Telefax: 02461/61-6103 · e-mail: zb-publikation@fz-juelich.de

Zusammenfassung

Diese Dissertation beschreibt die physikalischen Konzepte und die Realisierung von ultraschnellen Photodetektoren, die einerseits mit Verfahren gefertigt wurden, die kompatibel zur Silizium- CMOS- Technologie sind und die andererseits auch im nahen Infrarot- Wellenlängenbereich bis etwa 1550 nm eine akzeptable Quanteneffizienz aufweisen. Die Wellenlängen von 1300 und 1550 nm werden in der modernen Optokommunikation im Fernverkehr eingesetzt, weil die Glasfasern in diesem Bereich ihr Absorptionsminimum aufweisen. Weil das technologisch überragend wichtige Silizium wegen seiner Bandlücke eine Absorptions-Grenzwellenlänge von 1.1 μm aufweist, kann es nicht direkt als Detektormaterial eingesetzt werden. Die im allgemeinen verwendeten III/V- Halbleiter sind nicht kompatibel zur Siliziumtechnologie, können also nicht zusammen mit Silizium aufgewachsen werden. Deshalb werden in dieser Arbeit Silizium - Germanium - Legierungen und reines Germanium als absorbierende Schichten untersucht. Das photoempfindliche Halbleitermaterial (Semiconductor S) wird mit zwei Metallen kontaktiert: "MSM - Detektor". Beide Metallflächen bilden sperrende Schottky - Kontakte zum Halbleiter aus, die gegeneinander geschaltet sind und die den Wert des Dunkelstromes bei angelegter Vorspannung begrenzen sollen, weil jeweils eine Schottkydiode sperrt. Dagegen können sowohl die photogenerierten Elektronen wie auch die Löcher direkt die Elektroden erreichen, denn für sie ist keine Schottky - Barriere zu überwinden. So wird ein sehr schnelles Zeitverhalten des Detektors erreicht. Zwei verschiedene Wege wurden beschritten, um eine ausreichende optische Absorption bei 1500 nm zu erzielen: Zum ersten wurden SiGe Übergitter mit Hilfe der Molekularstrahlepitaxie (MBE) auf einkristallinen dünnen Schichten aus $CoSi_2$ aufgewachsen. In diesen Übergittern wächst SiGe mit hoher Ge- Konzentration auf. Zusätzlich ist in diesen Übergittern das SiGe stark elastisch verspannt ("strained undulating layer superlattice"). Dadurch ergibt sich eine Verringerung der Bandlücke und eine verbesserte Infrarotabsorption. Die aus diesem Material strukturierten Detektoren haben eine Quanteneffizienz von 5 % bei 1300 nm und 0.9 % bei 1550 nm. Diese Detektoren setzen die erwähnte epitaktische Schicht aus metallischem $CoSi_2$ als "vergrabenen" elektrischen Schottkykontakt ein und sind "vertikal strukturiert", weil der zweite Schottkykontakt über dem SiGe als Cr - Deckschicht ausgebildet ist. Die charakteristische Driftlänge der photogenerierten Ladungsträger zu den Kontakten ist "senkrecht" durch die SiGe- Schicht und beträgt entsprechend nur etwa 400 nm. Die kurze Weglänge ergibt einen sehr schnellen elektrischen Pulsanstieg. Das gemessene

Zeitverhalten ergab eine Puls - Halbwertsbreite von 9.4 ps bei 1550 nm. Diese Halbwertsbreite ist vor allem durch die relativ große Kapazität der Anordnung bedingt, denn die beiden Kontaktmetalle bilden einen SiGe - gefüllten Plattenkondensator mit sehr geringem Elektrodenabstand. Zum zweiten wurde versucht, reines Ge auf Si (111) aufzuwachsen. Um die wegen der Gitterfehlanpassung zwischen Si und Ge zu erwartende Ge - Inselbildung zu unterdrücken, wurde beim Wachstum in der MBE eine inerte Oberflächenbedeckung durch Sb eingesetzt (Sb wirkt als "surfactant", also etwa wie ein schützendes "Flußmittel"). Ge wächst unter der passivierenden Sb - Deckschicht in Lagen auf Si (111) auf, weil Sb die Oberflächendiffusion des Ge behindert. Weil dieses Epitaxieverfahren nur direkt auf Si (111) erfolgreich realisiert werden konnte, mußte auf die vergrabene $CoSi_2$ - Elektrode verzichtet werden. Statt dessen wurden zur Realisierung des Detektors nach Entfernung der Sb - Schicht ineinandergreifende Fingerelektroden aus Cr auf der Ge - Oberfläche aufgedampft. Weil die Finger durch Photolithographie strukturiert werden müssen, ergab sich ein minimaler Fingerabstand von 1500 nm. Diese Detektoren zeigten eine Quanteneffizienz von 13 % bei 1320 nm und 7.5 % bei 1550 nm. Das Zeitverhalten ist wegen des Fingerabstandes von 1.5 μm etwas langsamer: eine Halbwertsbreite von 12.5 ps wurde gemessen. Die elektrische Pulslänge ist in diesem Fall ausschließlich durch den Driftweg der Ladungsträger zu den Cr - Elektroden gegeben. Das sehr schnelle elektrische Pulsverhalten beider Detektorbauweisen ist jedoch sehr befriedigend und stellt jeweils einen Rekordwert dar.
Die elektrischen Kurzzeitmessungen wurden auf einem eigens für diese Arbeit umgebauten optischen Femtosekunden- Spektroskopie- Messplatz durchgeführt. Ein Ti:Saphir - Festkörperlaser liefert ultrakurze Pulse von 120 fs Halbwertsbreite und 780 nm Wellenlänge, die in einem nachgeschalteten optischen parametrischen Oszillator (OPO) mit Hilfe nicht- linearer Prozesse zu kurzen Pulsen längerer Wellenlänge (1300 - 1550 nm) konvertiert werden. Diese optischen Pulse wurden auf die Detektoren fokussiert. Das elektrische Signal der Detektoren wurde über eine Mikrostreifenleitung abgeleitet und mit Hilfe eines elektrooptischen $LiTaO_3$ Kristalles optisch ausgewertet ("Optical pump- probe set-up").

Abstract

This thesis presents two different concepts for the fabrication of ultrafast metal-semiconductor-metal (MSM) photodetectors, which are to be used in the near-infrared wavelength regime and which are compatible to silicon processing techniques. To achieve this goal, we have grown Si-$Si_{1-x}Ge_x$ undulating layer superlattices with x=0.39 and 0.45 by molecular beam epitaxy (MBE) on top of epitaxial implanted $CoSi_2$ layers and fabricated "vertical" MSM detectors. The devices show a quantum efficiency of 5% for the wavelength of 1320 nm and 0.9 % for 1550 nm. We performed time response measurements, using a Ti:sapphire laser and an optical parametric oscillator which generates ultrafast pulses at infrared wavelengths. An electrical response time of 11.6 ps full width at half maximum (FWHM) was obtained at a wavelength of 1300 nm. At 1550 nm a response time of 9.4 ps was measured.
In a second approach, we have grown pure Ge by MBE on Si (111). The sensitive volumes are 270 nm thick Ge films. Interdigitated Cr metal top electrodes of 1.5 - 3 μm spacing and identical finger width form Schottky contacts to the Ge film. These detectors show a response time of 12.5 ps full width at half maximum both at 1300 nm and 1550 nm. The temporal response is limited by the transit time of the carriers between the electrodes.

Contents

Chapter 1

Introduction

Ultra-fast photodetectors in the wavelength range from 0.8 μm to 1.6 μm are in the focus of interest, since lightwave communication systems are moving towards data transmission rates beyond the 10 Gbit/s regime. In addition, the existence of ultrashort optical pulse sources as well as the rapidly growing capabilities of electrical and optical sampling systems create a demand for optoelectronic converters which cover a bandwidth of up to 100 GHz. Ultrashort response times (<10 ps) and bandwidts in the range of 40 to 100 GHz in the near-infrared have been demonstrated so far with vertical *p-i-n* or Schottky photodetectors making use of InGaAs as photosensitive material. The need for monolithic integration of optoelectronic circuits has stimulated appreciable research activities directed toward the development of ultra-fast photodetectors which can be easily fabricated and which are compatible with the silicon CMOS processes. Lateral interdigitated photodetectors of the metal-semiconductor-metal (MSM) type meet this requirement. Besides the ease of fabrication, lateral photodetectors offer a lower device capacity in comparison with vertical detectors of identical size of the active area. In the near-infrared wavelength range up to 1550 nm MSM photodetectors are the most promising candidates.

Ge and $Si_{1-x}Ge_x$ are excellent materials for fabrication of near-infrared detectors, due to their absorption properties. The epitaxial growth of Ge on Si, however, has to overcome the lattice mismatch of 4.2 % between Si and Ge. Dislocation free Ge or $Si_{1-x}Ge_x$ can be grown up to a certain critical thickness only. Since Si and Ge are completely miscible, random alloys of any composition can be made. In order to obtain good responsivity for wavelengths around 1550 nm, $Si_{1-x}Ge_x$ layers with large Ge concentrations are required. However, their thickness has to remain under a critical value, which decreases rapidly with increasing the Ge content. In spite of this constraint photodetectors using $Si_{1-x}Ge_x$ alloys have been successfully fabricated. The

performances of these devices are excellent at 1300 nm but rather poor at 1550 nm. The concept for the fabrication of high performance SiGe detectors, which is presented in this thesis, is based on a plate capacitor structure with SiGe as the dielectric material. The SiGe detectors have a novel type of structure: *the undulating layer superlattice*. By adopting this technique, a substantially higher concentration of Ge can be incorporated into Si, thereby relaxing the dependence of the critical layer thickness or the Ge concentration As an alternative to SiGe layers, pure Ge layers can be grown on Si or SiGe buffer layers by special techniques to keep the dislocation density sufficiently low. MSM detectors using pure Ge on Si deposited at low temperature by chemical vapor deposition method were fabricated. The response speed of this detectors was in the nanosecond range.
In this thesis a systematic analysis of the high performance potential of two different MSM designs is presented:

1. A plate capacitor design with an epitaxial $CoSi_2$ layer as the bottom electrode

2. An interdigited design using the surfactant mediated growth of a Ge film on Si (111) in an MBE system.

The thesis is organized as follows: In Chapter 2, a short description of the metal-semiconductor contact is given. The basic concept of a Schottky detector and a metal - semiconductor - metal detector is presented. Chapter 3 introduces the measurement system used for the detectors' response time analysis. The femtosecond spectroscopy and electro-optical sampling methods are explained. Chapter 4 is dedicated to vertical SiGe superlattice MSM detectors. After an introduction to the SiGe alloy material, the material quality and the detector's fabrication processes are presented. In the second part of the chapter, dc- characterization and time response measurements are explained and compared with similar Si and SiGe structures. The metal-germanium-metal (MGeM) photodetectors are discussed in Chapter 5. First the growth technique and the material quality are presented, followed by the detector fabrication processes. The importance of a good passivation of the surface for the reduction of the device leakage current is underlined. Details of the temporal evolution of the current response are analyzed as a function of the applied voltage, the electrode spacing, the wavelength and the illumination intensity. Chapter 6 compiles the results and achievements of this work.

Chapter 2

Si-based photodetectors

In this Chapter, an introduction into Si-based detectors is given. The Schottky detector and the theory of Metal-Semiconductor-Metal detectors are presented at the beginning, after an analytical description of a metal semiconductor junction. In the second part of the chapter the heterostructure detectors and their energy band alignment are presented.

2.1 Schottky contact

2.1.1 Energy band relaxation

The junction between a metal and an intrinsic semiconductor forms a Schottky contact. A barrier is formed at the metal-semiconductor interface. When a metal is making an intimate contact with a semiconductor, the Fermi levels in the two materials must be coincident at thermal equilibrium. Figure 2.1 shows the electronic energy relations at an ideal contact between a metal and a $n-$type semiconductor in the absence of surface states.

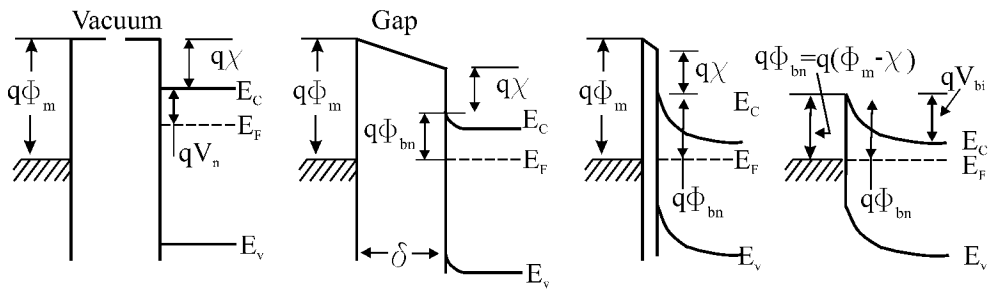

Figure 2.1: Energy band diagram of a metal semiconductor contact [1].

At left, the metal and semiconductor are not in contact, and the system is not in equilibrium. If a wire is connected between the metal and semiconductor, the charge will flow and thermal equilibrium is established. The Fermi level on both sides line up. Relative to the Fermi level in the metal, the Fermi level in the semiconductor is lowered by an amount equal to the difference between the two work functions. The work function is the energy difference between the vacuum level and the Fermi level and for a metal it is denoted by $q\Phi_m$ (in volts) and is equal with $q(\chi+V_n)$ in the semiconductor, where $q\chi$ is the electron affinity and the qV_n is the energy difference between E_c and the Fermi level. As the distances δ decrease, an increasing negative charge is build-up in the semiconductor and a positive charge is distributed over a barrier region near the semiconductor surface. When the δ is comparable with the interatomic distance, the gap becomes transparent to the electrons and a limiting case is obtained (Fig. 2.1 right). The limiting value of the barrier height is given by:

$$\Phi_{Bn} = \Phi_m - \chi_s \tag{2.1}$$

The barrier height is simply the difference between the metal work function and the electron affinity (χ). For a $p-$type semiconductor the ideal barrier height is:

$$\Phi_{Bp} = E_g - (\Phi_m - \chi_s) \tag{2.2}$$

This barrier height is valid for an ideal metal-semiconductor contact. Different effects like surface quality of the semiconductor, defects in the semiconductor, Schottky barrier lowering effect (see subchapter 2.1.2) affect the barrier height. In Table 2.1 the most reliable Schottky barrier height values for Cr and $CoSi_2$ metals on clean silicon surfaces are presented.

Typ	Cr	$CoSi_2$
n-silicon	0.61	0.64
p-silicon	0.51	0.46

Table 2.1: Schottky barrier height (in eV) for Cr and $CoSi_2$ on silicon(from [1])

2.1.2 Schottky effect

The Schottky effect is the lowering of the potential energy for charge carrier emission when an electric field is applied (Fig. 2.2).

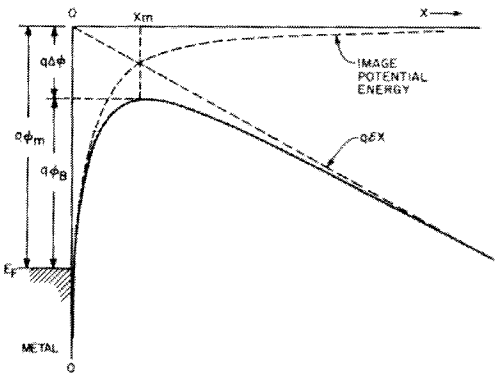

Figure 2.2: Energy band diagram between a metal surface and a vacuum. The effective work function is lowered when an electric field is applied to the surface.

When an electron is at a distance of x from the metal, a positive charge will be induced on the metal surface. The attractive force F, between the electron and an equal opposite charge is:

$$F = \frac{-q^2}{16\pi\epsilon_s x^2} \tag{2.3}$$

where ϵ_0 is the primitivity of the space. The potential energy of an electron at a distance x from the metal surface, shown in fig 2.2, is given by:

$$E_{pot} = \frac{q^2}{16\pi\epsilon_s}\int_x^\infty \frac{dx}{x^2} = \frac{q^2}{16\pi\epsilon_s x} \tag{2.4}$$

When an external field E is applied, the Schottky barrier lowering $\Delta\Phi_{bi}$ is obtained by minimizing of the total potential energy ($dE_{pot-total}/dx=0$):

$$\Delta\Phi_{bi} = \sqrt{\frac{q\mathcal{E}}{4\pi\epsilon_s}} \tag{2.5}$$

2.2 Current transport processes

The current transport in metal-semiconductor contacts is mainly due to majority carriers. Fig 2.3 shows four basic transport processes under forward bias.
The four processes are:

- Transport of electrons from the semiconductor over the potential barrier into the metal

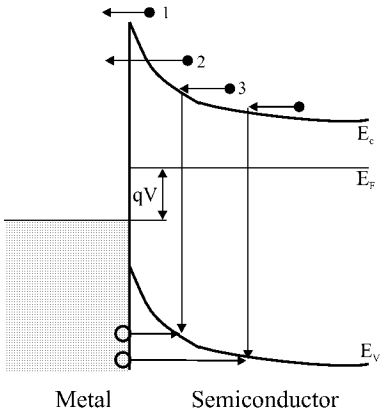

Figure 2.3: Basic transport processes over a Schottky-barrier [1]

- Quantum-mechanical tunneling of electrons through the barrier
- Recombination in the space charge region
- Hole injection from metal to semiconductor

In addition, we may have edge leakage current due to a high electric field at the contact periphery or interface current due to traps at the metal-semiconductor interface. For high mobility semiconductors (e.g. Si, Ge) the transport can be described by the Bethe's thermionic emission theory [3]. This theory is derived from the assumption that

1. the barrier $q\Phi_{Bn}$ is much larger than kT
2. thermal equilibrium is established at the plane that determines the emission
3. the existence of a net current flow does not affect this equilibrium.

The current density J_{sm} from the semiconductor to the metal is given by the concentration of electrons with energies sufficient to overcome the potential barrier:

$$J_{sm} = \int_{E_F+q\varphi_{Bn}}^{\infty} qv_x dn \tag{2.6}$$

where $E_F + q\Phi_{Bn}$ is the minimum required energy for thermionic emission into the metal, v_x is the carrier velocity in the transport direction. If a bias V is applied, the current which flows from Si to metal is:

$$I_{sm}(V) = AA^*T^2 e^{\frac{-q\Phi_{Bn}}{k_B T}} \cdot e^{\frac{qV}{k_B T}} \tag{2.7}$$

where A is the detector area and A* is the effective Richardson constant and k_B is Boltzamann constant [1]. Since the barrier height for electrons moving from metal into the semiconductor remains the same, the current flowing into the semiconductor is unaffected by the applied voltage. It is equal to the the current flowing from the semiconductor into metal when thermal equilibrium prevails. (i.e. V = 0).The current is then

$$I_{ms}(V) = AA^*T^2 e^{\frac{-q\Phi_{Bn}}{k_B T}} \tag{2.8}$$

The total current is then obtain by adding the currents in both the directions:

$$I(V) = I_s \left(e^{\frac{qV}{k_B T}} - 1 \right) \qquad \text{and} \qquad I_s = AA^*T^2 e^{\frac{-q\Phi_{Bn}}{k_B T}} \tag{2.9}$$

2.2.1 Schottky photodiodes

Schottky photodiodes are metal-semiconductor devices. The theory of Schottky diodes was reviewed in [2]. Schottky diodes extend the spectral sensitivity range beyond the cut-off wavelength of 1.1 μm of silicon into the infrared spectral range. Furthermore, they may increase the efficiency of silicon-based photodetectors in the blue and ultraviolet spectral range. Schottky diodes consist of a metal-semiconductor contact. The metal, however, can be replaced by a silicide. $PtSi_2$, $TiSi_2$, IrSi and $CoSi_2$ are the most frequently used silicides in device fabrication. Usually, good Schottky diodes are obtained for silicon with a doping level under 10^{16} cm^{-3}. The detectable energy in the infrared spectral range due to absorption of photons in the metal or in the silicide and the generation of hot carriers, which can overcome the energy barrier Φ_B and enter into the silicon (see Fig. 2.4), is:

$$\Phi_B < h\nu < E_g \tag{2.10}$$

This process is called *internal photoeffect*. However, for ultra-fast application in the range of 1.3 μm $-$ 1.5μm in devices at room temperature and with low reverse current, the quantum efficiency is very low (maximal 0.1%).

2.3 Metal-Semiconductor-Metal detectors

A metal-semiconductor-metal detector consists essentially of two back-to-back Schottky diodes. At any time one of the Schottky contacts is in the reverse bias condition. For a low dark current, a large enough barrier of the metal-semiconductor junction is necessary. If the same metals are used for the two contacts, the currents which flow through the structure by changing

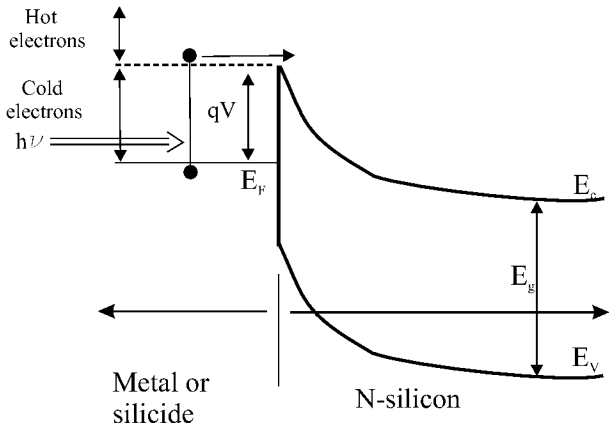

Figure 2.4: Energy band diagram of a Schottky photodetector on n-type Si.

the applied bias are equal. In Fig 2.5 the band diagram and the current flows are shown for a non-symmetrical structure. As we can see in the Fig. 2.5, the total current, I_t, is obtained by adding the electron and hole currents for both contacts:

$$i_t = i_1 + i_2 + i_3 + i_4 \qquad \text{with} \qquad i_i = AA^*T^2 \exp\left(\frac{q\Phi_{effi}}{k_B T}\right) \tag{2.11}$$

Every current in the equation 2.11 is a function of the effective Schottky barrier $\Phi_{eff,1-4}$, which represents the potential barrier which should be overcome by the carriers to enter from the metal into semiconductor. Under the influence of the applied voltage, the effective Schottky barrier is decreased and higher currents can flow through the structure. Further, under the applied voltage, from the carriers which can overcome the Schottky barrier, only those carriers which are moving in the electrical field direction will contribute to the total current. For a voltage V < 0 applied to contact 1, $i_t = i_1 + i_4$ and for a voltage V > 0, $i_t = i_2 + i_3$. The dominant contribution to the current is given by the lowest Schottky barrier potential, and as we can see in Fig. 2.5 $i_t = i_4$ for V < 0 and $i_t = i_3$ for V > 0. Due to the asymmetry of the Schottky contacts, a build in potential (V_{bi}), also called the flat band potential is present in the structure (Fig. 2.5(b) and a current flow even at 0 V applied bias. If a voltage of $-V_{bi}$ is applied to the structure, the flat band condition is obtained. In this case no electrical field is present in the structure. This case is presented in fig 2.5(c). The current which is flowing

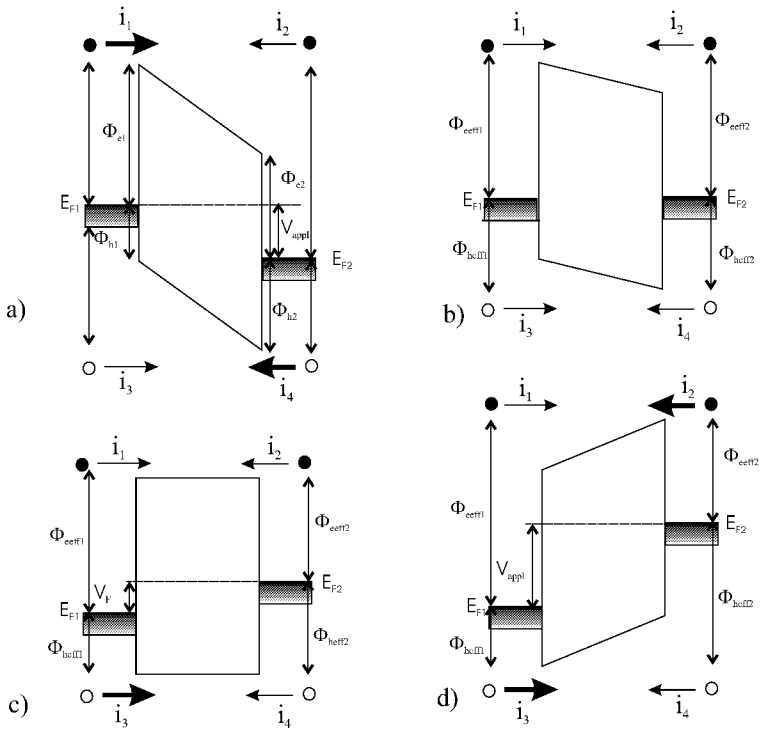

Figure 2.5: Current flow in a MSM structure.

through the MSM structure is given by:

$$I_{MSM} = \frac{I_{s1}I_{s2} \cdot (e^{(\frac{qV}{k_BT})} - 1)}{(I_{s2} + I_{s1} \cdot exp(\frac{qV}{k_BT})) + \frac{V}{Rp}} \tag{2.12}$$

where $I_{s1,2}$ are given by the equation 2.8.
Two designs are used for fabricating MSM photodetectors: a planar design, using interdigitated electrodes and a vertical design using a buried metal layer. Of those two, the planar contact arrangement has the advantage of higher speed.

2.4 Semiconductor heterostructures and superlattices

Using modern epitaxial methods, such as molecular beam epitaxy (MBE) or chemical vapor deposition (CVD) it is possible to deposit different semiconductors on one another in a crystalline form. These semiconductors will

generally have different electronic properties and in particular different electronic band gaps. Such layered structures play a particularly important role in devices made from III - V semiconductors such as GaAs, InP, but also Si-based devices. Structures consisting of layers of two different semiconductors grown epitaxially on one another are called *heterostructures*. If one semiconductor is sandwiched between two barrier layers (e.g. Si/SiGe/Si) a quantum well structure is formed. The term *multiple quantum wells* (MQW) refers to structures where the wells are isolated from each other by a relatively thick barrier region. If the barrier layer is thin, so, that there is an appreciable interaction between the wave-functions in the neighboring wells, the structure is called a *superlattice* (SL).

2.4.1 Band alignment for SiGe/Si heterostructures

In a heterostructure, matching of the two band structure takes place within an atomic distance. Interatomic forces and energies are decisive for this process and the electric fields are of the order of the atomic field ($\geq 10^8$ V/cm). The band banding, on the other hand takes place over hundreds of Angstroms, so at thermal equilibrium, the Fermi level has the same value on both sides of the semiconductor interface. The most important material related parameters of a semiconductor heterostructure are therefore, the valence and conduction band discontinuities. Until the work of Margaritondo et al. [4], no clear picture existed for the expected band alignments and band offsets for (Ge, Si) system. The first estimates of ΔE_v for a pseudomorphic Ge/Si heterointerface were obtained by Van de Walle and Martin [5]. For (001) oriented interfaces ΔE_v for Ge on Si was calculated for three cases, corresponding to :

- growth on Si substrates (cubic Si and strained Ge)
- growth on Ge substrate (cubic Ge and strained Si)
- growth on on $Ge_{0.38}Si_{0.62}$ (both Si and Ge strained)

Their result indicates that the Ge valence band edge lies above the Si valence band edge in all of the above cases. If the effect of alloying is included via a linear interpolation, then ΔE_v on (001)(Ge, Si) is well described by the relation:

$$\Delta E_v[(Ge, Si)/Si] = (0.74 - 0.53 \cdot x_s)x \tag{2.13}$$

where x denotes the Ge content in the epilayer and x_s denotes the Ge content in the substrate.

The strain dependence of the bandgap has been combined with the strain and alloy dependence of ΔE_v in order to determine the band alignment for three distinct cases:

- growth of $Ge_{0.2}Si_{0.8}$/Si heterojunctions on (001) Si substrates
- growth of $Ge_{0.5}Si_{0.5}$/Si heterojunctions of equal thickness on an unstrained (001) $-$ $Ge_{0.25}Si_{0.75}$ buffer layer, and
- growth of $Ge_{0.5}Si_{0.5}$/Si on (001)Si substrates.

These results are given in the Fig. 2.6(a),(b)and(c) respectively, clearly indicate that the type of band alignment and the value of ΔE_c for pseudomorphic Ge_xSi_{1-x}/Si heterointerfaces are sensitive to the state of the strain in the Si epilayers.

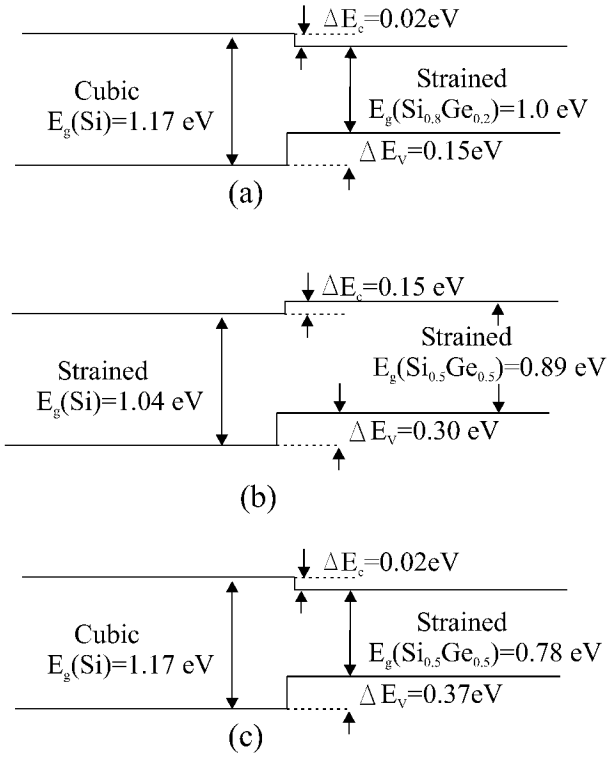

Figure 2.6: Band alignment for (a) $Ge_{0.2}Si_{0.8}$/Si heterojunctions on (001) Si substrates, (b) $Ge_{0.5}Si_{0.5}$/Si heterojunctions on (001) $-$ $Ge_{0.25}Si_{0.75}$ substrate, (c) $Ge_{0.5}Si_{0.5}$/Si on (001)Si.

2.4.2 SiGe infrared devices

The most prominent type of Si-based heterostructure detectors is the heterojunction internal photoemission (HIP) detector [9]. This detector consists of a thin, degenerately p-doped SiGe layer on p-Si substrate, (Fig 2.7).

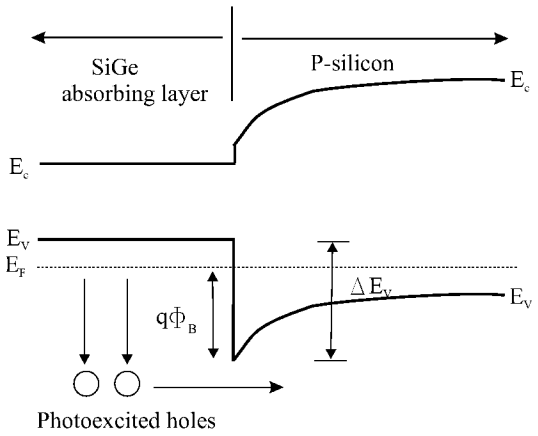

Figure 2.7: Energy band diagram of a p_+-SiGe/p-Si HIP detector, [9]

The detection in the infrared involves absorption of photons in the p^+-doped SiGe layer, creating hot holes which are collected in the p-Si through the internal photoemission over the SiGe heterojunction barrier. Free carrier absorption is the main mechanism and thus a very high doping level in the SiGe layers is chosen. The hole current can be described by the the thermoionic-emission theory formula:

$$I = AA^*T^2e^{\frac{-\Delta E_{eff}}{k_BT}} \tag{2.14}$$

where ΔE_{eff} is the effective, electrical barrier height, aproximated by [6]:

$$\Delta E_{eff} = \Delta E_V(SiGe) + \Delta E_V(B) - (E_V - E_F). \tag{2.15}$$

$\Delta E_V(SiGe)$ is the valence band offset of the heterostructure which depends only on the Ge concentration, $\Delta E_V(B)$ the heavy doping bandgap narrowing and $(E_V - E_F)$ is the band filling due to electrically active boron. The cutoff wavelength is given by the Δ_{eff} barrier height. The HIP detectors resemble in many aspects the Schottky barrier detectors. In both cases the current can be described by the thermoionic-emission formula 2.15 and the escape depth of the photogenerated carriers is related to the mean free path of the hot carriers. In order to increase the quantum efficiency a MQW structure

with many SiGe absorption layers and Si barrier layers is used. The narrow bandgap SiGe layers function as quantum wells in confining carriers. The hole density in undoped SiGe layers is increased if the Si barrier layers are p-type doped. A complete description of quantum well infrared detectors can be found in [8]. The heterojunction LWIR (longwave infrared) photodetectors offer a higher quantum efficiency compared with silicide Schottky-barrier detectors. One reson is the narrow band of occupied hole state in the P^+-SiGe layers in the LWIR detectors. In the Schottky detectors, photons can excite carriers far below the Fermi energy level which cannot gain sufficient energy to overcome the barrier to the Si. Only a small part of the photoexcited carriers (near the Fermi level) can exceed the Schottky barrier energy. The quantum efficiency rises only slowly with the photon energy above the potential barrier. The narrow band of absorbing states in the P^+-SiGe layer of the heterojunction LWIR detector, in contrast, leads to a sharp turn-on, which means higher responsivities close to the cutoff wavelength.

Chapter 3

Femtosecond pump-probe spectroscopy

In semiconductor microelectronics, small distances and high speed are closely related. Transistors with base lengths of only a few tens of nanometers have electron transit times of less then one picosecond. To develop high speed devices, one must understand the dynamical properties of charge carriers in semiconductor on picosecond and femtosecond time scales. Currently high-speed measurement techniques are either done in the optical domain (transient luminescence), the electrical domain, or a combination of the two (photodiode response measurements). As progress is made towards the THz frequency range in a number of fields all-optical or opto-electronic techniques are gaining on electrical techniques. High speed optical techniques are now used effectively in areas that were once the domain of electrical techniques. High-speed sampling oscilloscopes are being superseded by electro-optic sampling systems. This chapter describes the electro-optic sampling technique used in analysis of non-equilibrium phenomena in semiconductors. Since an optical parametric oscillator is used in the present work for wavelength conversion, the principle of this technique is briefly described.

3.1 Electro-optic sampling

It has been demonstrated in the literature that electro-optic sampling is an excellent technique to measure the longitudinal electric field profile of both optical [10] and electron pulses [11]. The electro-optic sampling technique is based on the linear electro-optic effect (also known as Pockels effect) [12]: when an electric field is applied to an electro-optic crystal, it induces birefringence. In our case the birefringence is induced by an electrical pulse given

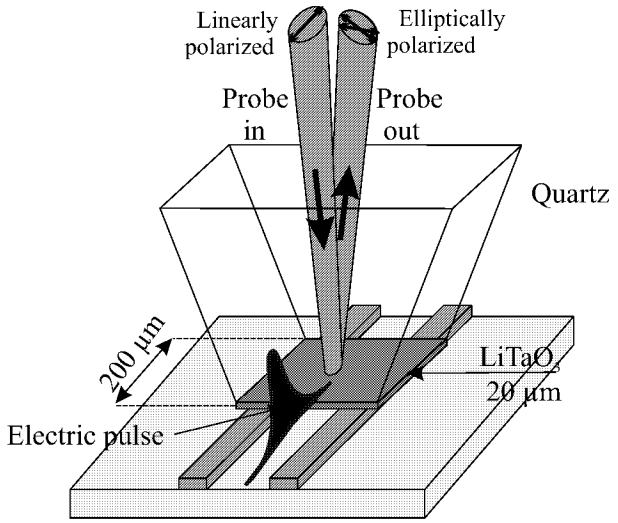

Figure 3.1: Electro-optic sampling process

by the photodetector under light excitation. The birefringence can then be probed by a synchronized, ultrashort Ti:sapphire laser pulse Fig. (3.1). The induced birefringence causes the initially linearly polarized optical probe beam to acquire a phase difference between its polarization parallel and perpendicular to the induced optical axis of the sensor crystal, and therefore the probe beam will become elliptically polarized. The degree of ellipticity can then be measured by using suitable polarization optics. By scanning the delay between the Ti:Sappire pump and probe pulses, a cross-correlation of the incident electric field pulse is obtained. Note that with this electro-optic detection technique, an asymmetric pulse shape can be measured with sub-picosecond time resolution and without ambiguity. Furthermore, information about the electric field, including its sign, is obtained, in contrast to most other techniques that yield information on the intensity only.

Our measurements were performed with an electro-optical $LiTaO_3$ crystal produced by Terametrics company. This crystal which has a high electro-optic coefficient, can be single domain grown and is very stable at room temperature. The crystal is glued on a pyramid shape quartz carrier. The c-axis of the crystal is oriented perpendicular to the microstrip transmission line. Without the influence of an external electrical field it displays no birefringentce effect and has a low polariton resonance frequency of 0.95 THz.

3.2 Parametric oscillations

In linear optics, it is assumed that the applied optical field is sufficiently weak so that the induced polarization $\vec{P}$(t)depends linearly on the applied electrical field strength E(t) such that:

$$\vec{P} = \epsilon_0 \chi^{(1)} \vec{\mathcal{E}}(t) \tag{3.1}$$

where the constant of proportionality $\chi^{(1)}$ is the linear susceptibility. When the applied field is sufficiently strong, one can often describe the induced polarization as a power series in the applied field strength such that:

$$\vec{P} = \epsilon_0 (\chi^{(1)} \vec{\mathcal{E}} + \chi^{(2)} \vec{\mathcal{E}}^2 + \chi^{(3)} \vec{\mathcal{E}}^3 + ...) \tag{3.2}$$

where the $\chi^{(2)}$ and $\chi^{(3)}$ are known as the second and the third-order nonlinear susceptibilities. The two lowest order nonlinear terms, which are displayed in equation 3.2, are responsible for most of the nonlinear optical interactions. Second-order nonlinearities are commonly employed to generate new frequency components from one or more incident laser beam.Optical parametric oscillators based on difference frequency generation are routinely used to generate frequency-tunable radiation throughout the optical spectrum [19]. The basic nonlinear frequency generation processes are:

1. Sum frequency generation, Fig. 3.2(a)
2. Difference frequency generation, Fig. 3.2(b)
3. Parametric oscillation, Fig. 3.2(c)

3.3 The laser system

The heart of the measurement system is the passive mode-locked Ti:sapphire laser [13] pumped by an Ar^+-ion laser (Innova 400, made by Coherent [14]) at a wavelength of $\sim$ 500 nm. The Ti:sapphire laser produces pulses of 120 fs FWHM (Full Width at Half Maximum) at a repetition rate of 76 MHz with an average power of 1.8 W. The central wavelength of the laser can be adjusted from 700 nm to 920 nm using a birefringent filter in the laser cavity. For detector characterization in the IR radiation range an additional Optical Parametric Oscillator (OPO) is added to the measuring system. It is pumped by the Ti:sapphire laser. The OPO is a resonant oscillator which uses a nonlinear crystal as the active medium. When the pump pulse is focused on the crystal two pulses with different wavelengths are generated:

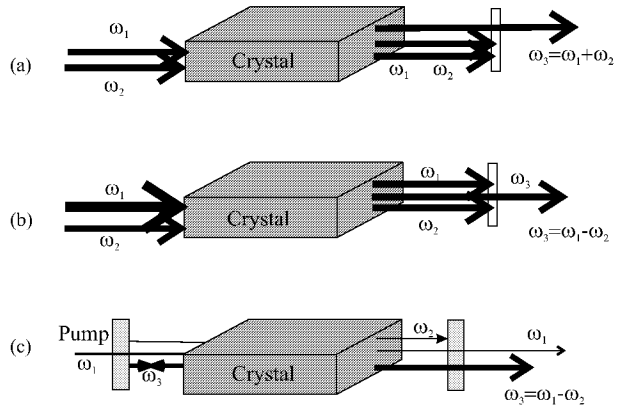

Figure 3.2: Parametric oscillation

the *idler* (ω_2) and *the signal* (ω_3). By the use of a narrow band reflectance mirrors, the *signal* pulse wavelength alone can be amplified (the idler would be transmitted at the mirrors), see Fig. 3.3. Since the OPO has no energy storage mechanism an amplification of the circulating *signal* pulses is possible only if these cross the nonlinear crystal at the same time as the pump pulse. Therefore the OPO resonator has to have exactly the same length as the

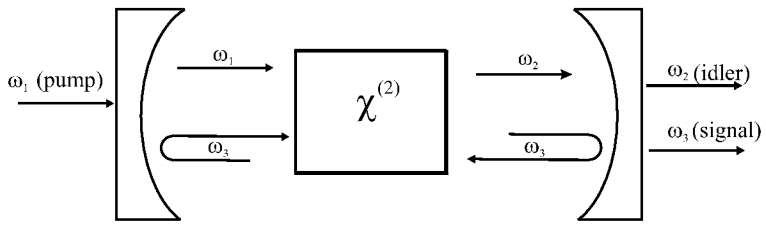

Figure 3.3: Schematic illustration of an parametric oscillator

Ti:sapphire laser resonator, so that they have the same repetition frequency. This technique is called synchronized pumping. There are different methods for tuning an OPO system:

- Temperature tuning
- Angle tuning
- pump wavelength tuning

In our system the tuning is made by changing the pump wavelength. The pump pulses are generated by the Ti:Sappire laser. Two nonlinear crystals are used for wavelength conversion:

- $KTiOPO_4$ crystal (KTP) for the wavelength range: 1000-1300 nm
- $CsTiOAsO_4$ crystal (CTA) for the wavelength range: 1300-1600 nm

The OPO system specifications for the two crystals are given in the table 3.1.

Crystal	KTP	CTA
Repetition rate	76 MHz	76 MHz
Wavelengths range	Pump 710...940 nm Signal 1040...1350 nm	Pump 735...790 nm Signal 1350...1600 nm
Laser power threshold	$<$ 0.5 Watt	$<$ 0.5 Watt
Output signal power	$>$ 200 mW at 1.25 W Pump	$>$ 150 mW at 1.25 W Pump
Spatial mode	TEM_{00}	TEM_{00}
Polarization state	Horizontal	Horizontal
Noise (rms)	$<$ 2 % limited by the pump laser and mechanical stability	$<$ 2 % limited by the pump laser and mechanical stability
Pulse duration	typ. 180 fs at 120 fs pump	typ. 180 fs at 120 fs pump

Table 3.1: Specifications for a KTP, CTA -optical parametric oscillator system

3.4 Femtosecond pump-probe set-up

Many of the all-optical high-speed techniques rely on the pump-probe technique. A high-speed event is stimulated by one laser pulse and the effect of this is measured by another laser pulse whose time of arrival is accurately known and can be varied. The pump and probe pulses are derived from the same laser source (Fig. 3.4), which is split into two. One half is the *pump* pulse and travels to the event via a fixed path. It is modulated by an acusto-optical modulator with a frequency of 97 kHz and then focused on the photodetector. By light absorbtion, electron-hole pairs are generated in the detector area which are separated by the applied electrical field, giveing rise to an electrical pulse in the microstrip transmission line. The build-up pulse passes the $LiTaO_3$ crystal, which is positioned directly over the strip line, changing the refractive indices of the crystal by electro-optic effect. The other half of the beam, the *probe* pulse, travels to the event via a variable path length and is focus on the measuring crystal. The *probe* pulse is back-reflected at the crystal's lower surface and the resulting change in its polarization state is further analyzed. The change in the *probe* polarization state is proportional to the electrical field strength and thus with

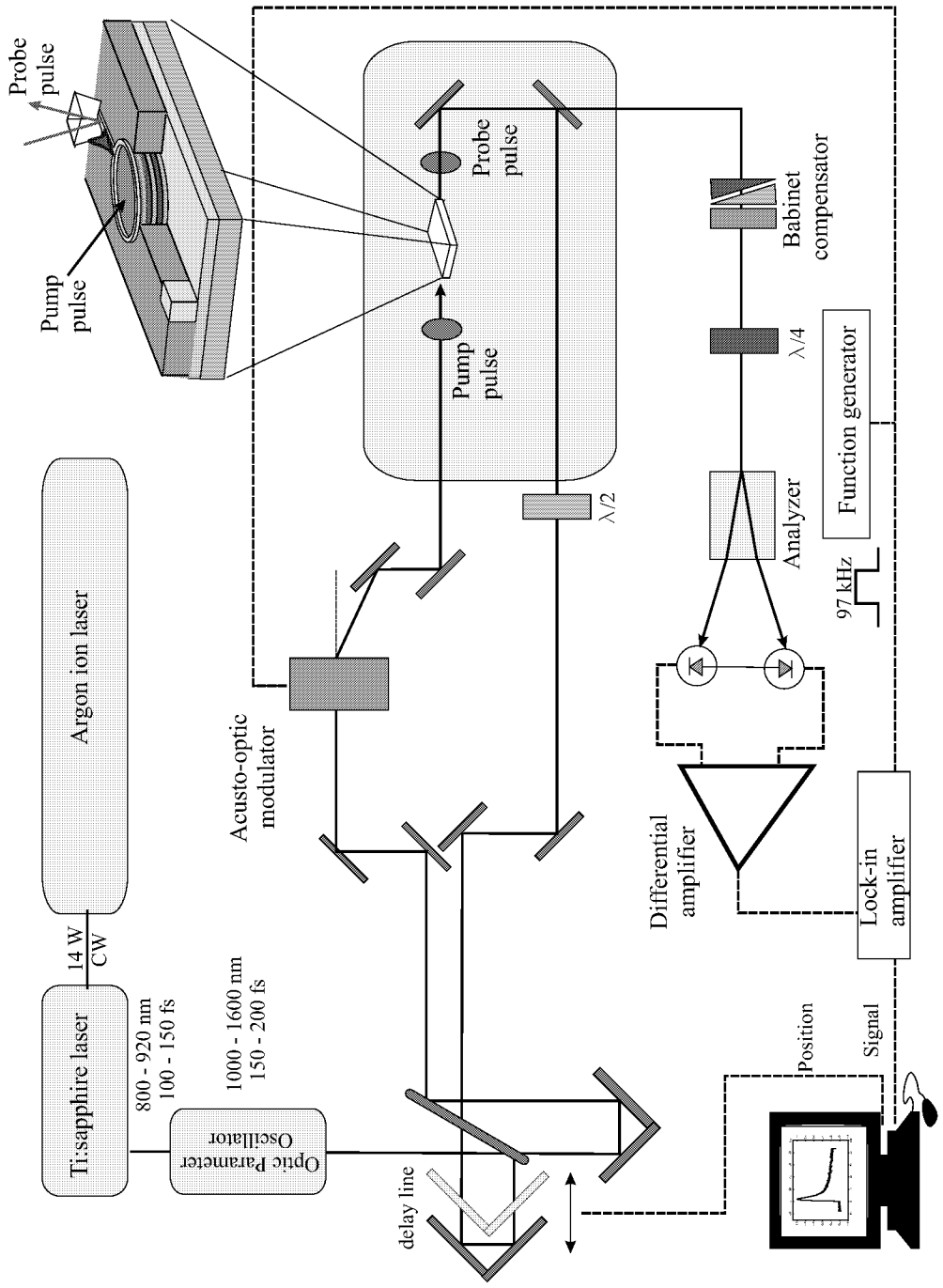

Figure 3.4: Femtosecond electro-optic set-up

the pulse height. The analyzer system consist of a Babinet compensator, a $\lambda/4$ waveplate and a Wollaston prism. The system converts the elliptically polarized probe pulse into two pulses with the polarization perpendicular to each other. The intensities of the resulting two pulses are measured with photodetectors. Their signal difference is then amplified by a factor of 2000 by a differential amplifier and detected with a phase-sensitive Lock-in amplifier. The modulation frequency of the acusto-optic modulator is used as reference signal. The output signal from the Lock-in amplifier is correlated with the delay time between the pump and probe pulses, by a computer. Using a well-known reference signal (e.g. 1 V) applied to the microstrip line the entire measurement set-up can be calibrated.

Chapter 4

SiGe superlattice MSM photodetectors

4.1 Introduction

Silicon is by far the most used material for the microelectronics and is well established as a cost effective, high quality substrate. Silicon wafer processing technologies for the production VLSI technology have also been standardized. There exists, however, a substantial potential for the integration of several optoelectronics functions to Si-based devices. The alloying of silicon with germanium allows a continuous change of the band gap [7] and thus a large variation of the refractive index and optical absorption. The lowest (fundamental) bandgap of coherently strained $Si_{1-x}Ge_x$ is shown in Fig. 4.1. The main limitation of the SiGe/Si system for photonic devices stems from the strain caused by a 4.2 % lattice mismatch between Ge and Si. This has been investigated extensively and it is well known that strain restricts the thickness and germanium concentration that can be incorporated into a fully strained MQW structure [15].
At large Ge concentrations (x>0.5) needed to extend the absorption wavelength to 1550 nm, the thickness of one strained SiGe layer which can be grown without dislocations is limited to 10-20 nm, depending on growth rate and temperature. The critical thickness for the introduction of dislocations is shown by the dashed line in Fig.4.2. Dislocations are generally fatal to electronic devices and cause large dark currents in photodetectors. In addition to the strain relaxation limit, for Ge concentrations higher than 25% surface rippling (Stranski-Krastanov growth) limits planar strained growth to a critical thickness even smaller than that for dislocations. This is shown by the solid line in Fig. 4.2. Therefore, there is a range of composition and thickness

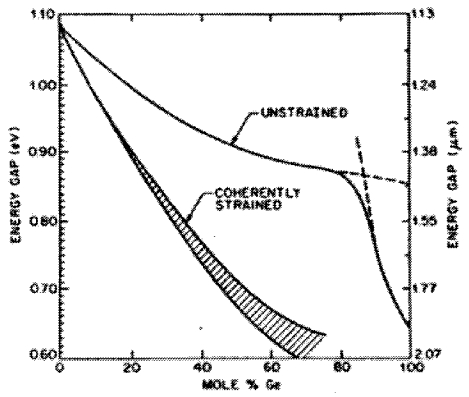

Figure 4.1: Bandgap for SiGe strained and relaxed structures versus Ge content [7]

values for which dislocation-free undulating layers can be deposited. Over the last few years, Stranski-Krastanov 3D growth of SiGe has been used to produce dislocation-free strained material, but optoelectronic devices have not been fabricated so far. The fabrication of a photodetector makes the optimisation of the growth parameters even more challenging, because the light absorption has to be sufficiently strong and the bandgap adjusted to the photon energy. Since SiGe quantum wells are thin compared to the thickness of the waveguide layer, the deposition of a multiperiod structure with a large number of repeats maximises the absorption coefficient at the wavelength of interest. However, the critical thickness for coherent growth becomes even smaller if more than one strained layer is grown in a multiple quantum well (MQW) structure. Therefore, one has to restrict the strained layer average thickness to smaller values when the number of periods in a MQW structure is increased. The smaller thickness (10 nm) in turn leads to a large quantum confinement shift that pushes the transition energy away from the band edge, making the 1550 nm target difficult to achieve. This limitation is illustrated by the dashed lines in Fig. 4.3 which shows the transition energy and wavelength in a typical planar SiGe/Si MQW structure as a function of the Ge content for 5 and 10 wells. For small Ge fractions, the thickness of each $Si_{1-x}Ge_x$ layer can be of a few tens of nanometers, in which case quantum confinement is negligible and the transition energy decreases as a function of Ge concentration (e.g., strained band gap). As the Ge fraction increases, the strain in the SiGe layers also increases and the critical thickness for defect-free growth decreases. This quantum confinement introduces a large energy

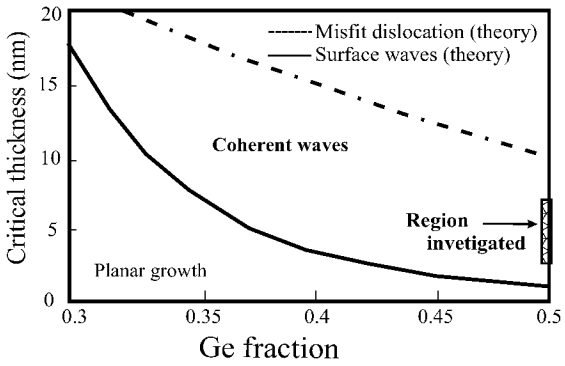

Figure 4.2: Critical thickness as a function of Ge fraction for planar growth, coherent waves, and dislocated waves respectively. The region investigated in this work is highlighted.(from [15])

shift which, for a structure with 10 periods, limits the transition wavelength to a maximum value of 1200 nm as shown for larger Ge fractions in Fig. 4.3. With a smaller number of periods, the critical thickness for each individual layer appears to be slightly larger, which allows for a slightly smaller confinement shift and thus a lower transition energy for N=5. The wavelength of 1300 nm turns out to be within reach if the number of periods in the MQW stack is limited to 5, but as explained earlier, light absorption in this case would occur in only a fraction of the thickness of a waveguide photodetector. The growth of absorbing material at 1550 nm thus appears very challenging if not impossible using strained planar growth. If undulating layers are used instead of planar growth, the larger thickness at the crest of undulations is expected to make quantum confinement shifts negligible. The solid line on Fig. 4.3 shows for comparison the strained band gap of SiGe (no quantum confinement), which is the transition energy expected from MQW structures realized with Stranski-Krastanov 3D growth. In order to realize photodetectors operating at 1550 nm it seems therefore desirable to realize coherent, defect-free multi-period structures with large concentrations of Ge while reducing quantum confinement energy shifts, in order to obtain transition energies closer to the strained band gap. The following paragraphs describe the procedure used to grow and characterize undulating $Si_{1-x}Ge_x$ MQW structures with band gap energies lower than 800 meV. For λ=1300 nm, Si-$Si_{0.5}Ge_{0.5}$ superlattice *p-i-n* diodes have been demonstrated in waveguide geometry [16] and for free beam incidence [17]. It has been shown that metastable Si-$Si_{0.5}Ge_{0.5}$ strained undulating superlattices with a transition energy of 0.8 eV, corresponding to a wavelength of 1550 nm can be grown

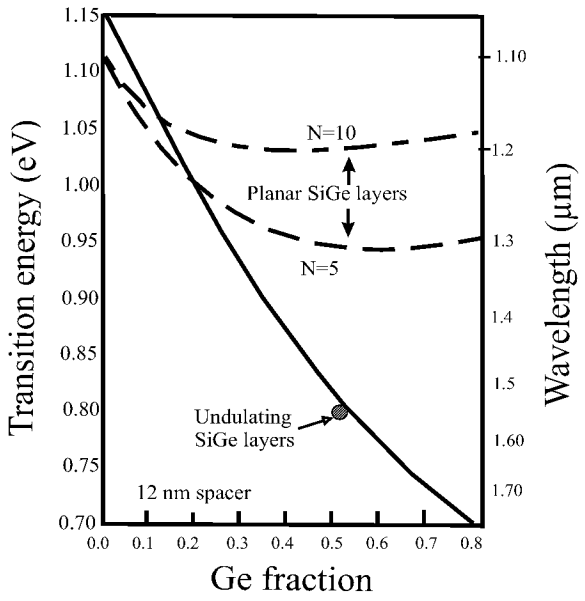

Figure 4.3: Transition energy and wavelength as a function of Ge fraction for MQW structures with 10 and 5 repeats with the maximum SiGe thickness allowing dislocation-free planar layers (dashed lines). Also shown is the strained band gap for thick SiGe, with no confinement shift (full line).(from [15])

with a low defect density [18, 20]. Recently photoluminescence at 1550 nm has been reported for Si-$Si_{0.5}Ge_{0.5}$ undulating layer superlattices grown by ultra high vacuum chemical vapor deposition [21]. We have extended the use of undulating layer superlattices to ultrafast Metal-Semiconductor-Metal (MSM) detectors, using a buried layer of epitaxial $CoSi_2$ as a bottom electrode. In the following paragraphs of this chapter the fabrication and the characteristics of these detectors will be presented and discussed.

4.2 Forming the buried $CoSi_2$ contact

The fabrication of a vertical MSM detector requires the presence of a buried metal contact under the semiconductor material. The emergence of silicides and the possibility of easy fabrication of buried metallic silicides opened-up new possibilities in microelectronics technology. Their potential includes high speed interconnects, buried collectors and bases for fast sub-micron devices. Of all the silicides, $CoSi_2$ is particularly attractive for applications as it has a low resistivity (typically$\sim$ 20-60 $\mu\Omega$·cm) and its simple cubic CaF_2 structure

is closely lattice matched to that of silicon (mismatch f = 1.20%). $CoSi_2$ layers fabricated by Ion Beam Synthesis (IBS) [22] offer several additional advantages over surface $CoSi_2$ layers grown by conventional means (e.g. molecular beam epitaxy (MBE)[23] and ultra high vacuum deposition). They show lower resistivities ($\sim$ 10-15 $\mu\Omega$·cm) and the ability to grow single crystal layers on all types of silicon substrates Si(100) and Si(111) [24].
IBS is a two stage process involving:

4.2.1 Co-implantation

$^{59}Co^+$ ions implantation were performed on 4 inch Si(100) wafers (ρ >1 kΩ·cm) with a medium current ion accelerator (EATON NV-3204) at elevated temperatures. The implantation energy was 200 keV. In order to prevent amorphization, the substrate temperature during implantation was 375 °C. To avoid channelling effects, the ion beam irradiation was carried out at 7° off the normal incidence. Using a dose of $2.2 \cdot 10^{17}$ Co/cm^2, $CoSi_2$ precipitates are formed in a depth of 70 nm in the Si wafer.

4.2.2 Annealing process

After Co implantation a subsequent high temperature annealing step helps to remove the residual radiation damage and facilitates the redistribution of the implanted species into a well defined compound layer. Prior to annealing, a 250 nm layer of SiO_2 was deposited onto the sample to protect the silicon surface during annealing. The annealing was performed in a N_2 atmosphere. The samples were heated up to 700°C and then the temperature was raised to 1150 °C within 30 s. At this temperature the sample was annealed for 20 s and in 12 s the temperature was decreased to 1000 °C and kept constant for 60 s. After this, the sample was cooled down to room temperature. As a consequence of thermal annealing at high temperatures large precipitates are formed at the peak position of the implantation profile. This process is called Ostwald ripening. During the later stages of the annealing coalescence of precipitates occurs and a high quality single crystalline buried $CoSi_2$ layer of 90 nm thickness is formed [23]. After annealing, the silicon oxide layer is removed in a HF solution (3 min. 30 s in AF91).

4.3 MBE growth of SiGe undulating layers

After annealing, some implanted wafers were sent to the National Research Council, Ottawa and processed in an MBE system to form the undulating

superlattices. These specimens consist of 10 periods with a nominal thickness of 12 nm for Si and 5 nm for SiGe, which are sandwiched between a 120 nm thick Si buffer layer and a 90 nm thick cap layer. The growth temperature was 630 °C. We will refer to these samples as SL-1.
The other part of the batch was further processed by our group in Jülich. After removing the oxide and performing an RCA cleaning procedure, (see appendix A.2) the wafers were processed in our MBE system (see appendix A.1). Heating up to 800 °C, while providing a small flux of Si desorbed the remaining SiO_2 on the surface. An additional 50 nm thick layer of pure Si was grown on top of the existing 70 nm Si buffer. We obtain 120 nm Si buffer between $CoSi_2$ and the following Si-SiGe superlattice. The superlattice grown has the same parameters as the Canadian samples (10 periods with nominal thickness of 12 nm Si and 5 nm SiGe). The growth temperature was 600 °C and it was not varied between the growth of Si and SiGe layers. The Si layers were grown at a rate of 0.15 nm/s, while for the SiGe layers a rate of 0.03 nm/s was used for both Si and Ge. The desired concentration was 50 % Ge in the SiGe layers. An additional 20 nm cap Si layer was grown on top of the superlattice. We will further refer to this samples as SL-2. The reason that we use Si buffer and cap layers was to conserve the good Schottky contacts between Si and metal contacts. Furthermore, a Si buffer layer increases the quality of the layers grown by MBE and the cap layer planarizes the structures surface.

4.4 Structural characterisation

4.4.1 Transmission Electron Microscopy (TEM)

In Fig. 4.4 cross-sectional transmission electron microscope (TEM) images of the two superlattices are shown. The dark area at the bottom of Fig. 4.4(a) is the $CoSi_2$ layer. The SiGe layers appear darker than the surrounding Si. Vertically ordered Ge-rich regions are visible in Fig. 4.4(a).
Such vertical ordering can be explained by a Stransky-Krastanov growth mode enhancement due to a local stress field developing in the vertical direction [25, 26]. Furthermore, threading dislocations extending from the $CoSi_2$ layer to the surface are visible. Fig. 4.4(b) and 4.4(c) show TEM images of parts of SL-2. The contrast in Fig. 4.4(b) highlights the material composition, while in the Fig. 4.4(c) the strain. Strong strain fields are visible around the Ge-rich regions. No threading dislocations are found within the resolution limit for this image. In comparison with SL-1 the Ge-rich regions of SL-2 seem to have smaller lateral and larger vertical dimensions.

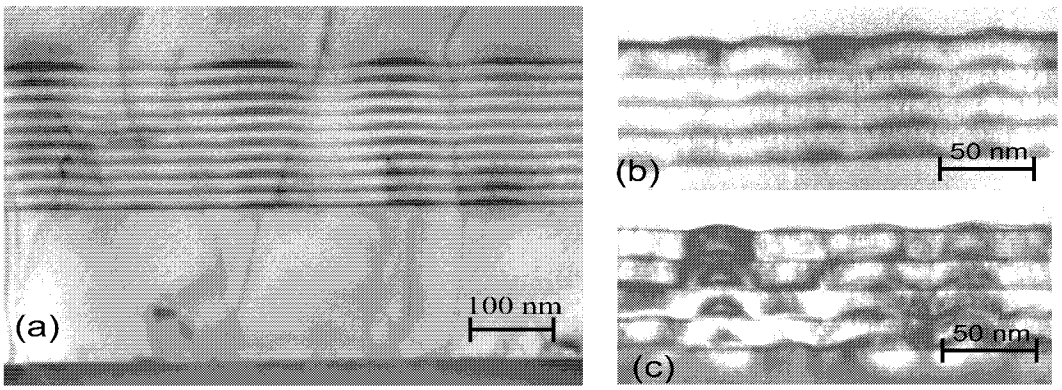

Figure 4.4: Cross-sectional TEM images of SL-1 (a) and SL-2 ((b) and (c)).

4.4.2 Rutherford backscattering spectroscopy (RBS)

Rutherford backscattering spectroscopy (RBS) and channeling were used to analyze the quality of the structures and the average Ge content of the layers. The spectra shown in Fig. 4.5 were measured with He^+ ions with an energy of 1.4 MeV under normal incidence. The channelling spectrum, also shown in Fig. 4.5(a), reveals a minimum yield of 6 %. The wavy layer structure influence not only the planar channeling but also the axial channeling. The minimum yields are always determined right after the surface peak. The values of 6 % for the minimum yield shows that the overgrowth of the wavy SiGe layers with Si did not lead to a perfect Si crystal lattice. This is what we also see clearly in the TEM pictures (Fig. 4.4(a)) with threading dislocations running all the way from the $CoSi_2$ to the top.

Eventhough it is predicted that such layers can in principle be grown *free of dislocations* [15] on pure Si wafer, it was difficult to achieve it in our case. One significant difference in the present case arises due to the presence of the $CoSi_2$ layer whose smaller lattice constant makes the problems related to stress more acute. Second, not all defects from the implantation are removed during annealing. In particular, one starts from a rougher surface than that provided by the virgin Si wafer, consequently adding to the problems related to epitaxy. The differences in the shape of the RBS spectra shown in Fig. 4.5 for the SL-1 and SL-2 samples are due to a thinner Si cap layer for the second sample. The He^+ ions lost less energy in the thinner Si cap layer and therefore the backscattering signal from Ge appears at higher energies/higher channel numbers than for the SL-1 sample. The signal from individual SiGe

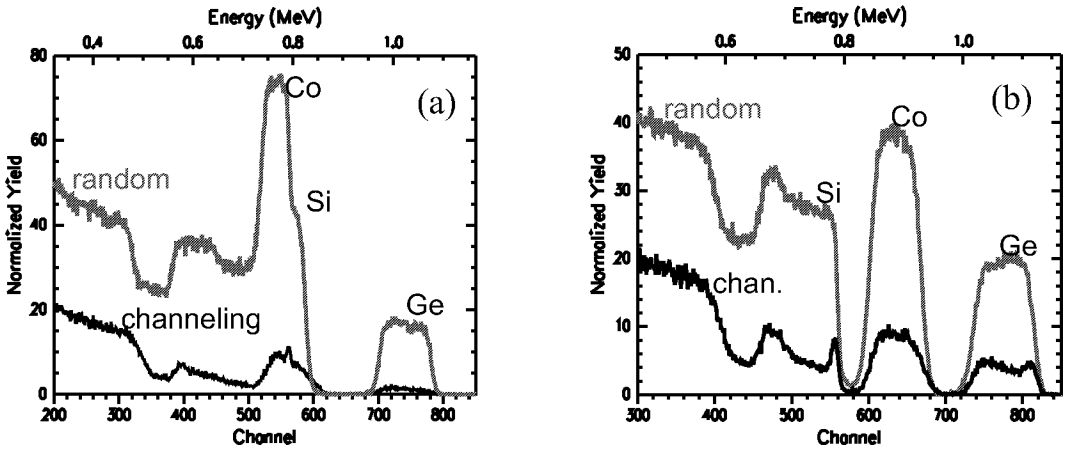

Figure 4.5: RBS and channelling spectrum in normal incidence geometry for SL-1 sample (a) and SL2-sample (b).

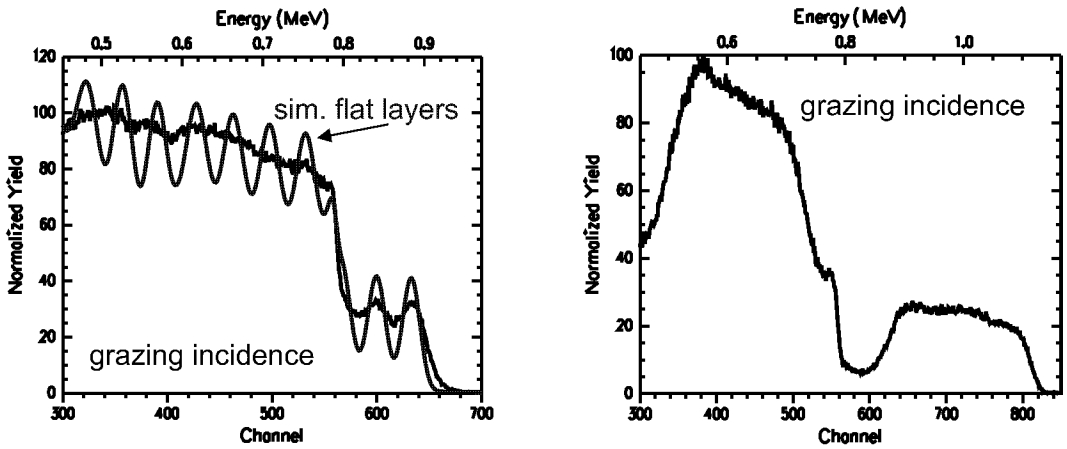

Figure 4.6: RBS Spectrum measured at grazing incidence (80°) and simulation for flat Si/SiGe layers.(a) SL-1 sample; (b) SL-2 sample.

layers could not be resolved, however, the yield due to Ge could be used to determine the average Ge content in the SiGe layers. The RBS spectrum in normal incidence revealed the total thickness of the superlattices and their average composition, as well as the thickness of the Si cap layer. Assuming that the calibration for the Si flux in the MBE was similar for the growth of the cap layer and the Si superlattice layers, the average Ge content of the SiGe layers can be calculated. We obtained a Ge content of 39 ± 2 % for SL-1 and 45 ± 2 % for SL-2. RBS measurements under 80° grazing incidence could partly resolve the superlattice layers of SL-1, but not of SL-2, see Fig.4.6. This confirms the higher vertical fluctuation of the SiGe layer in SL-2 observed in the TEM images. In Fig. 4.6(a) the spectrum is plotted along with a simulation for a $Si/Si_{0.61}Ge_{0.39}$ superlattice with sharp interfaces. Due to the undulating nature of the SiGe layers, the oscillations in the measured spectrum are less pronounced than in the simulation.

4.5 Detector fabrication

After the MBE growth of the superlattice the wafers were cut in 20 x 20 mm pieces and further processed in the Clean Room facilities.

4.5.1 Mesa etching and passivation

Using a photo-polymer and a positive lithography process (see appendix) the detector area is defined by a polymer mask. The structured polymer is then baked for 5 min at 150 °C for hardening. Introducing the sample into a Reactive Ion Etching System (RIE) (see appendix ??) and using SF_6 as the reactive gas, the unprotected Si is etched out until the $CoSi_2$ layer (Fig. 4.7(d)). In this way, pillars with diameters from 10 μm - 100 μm are defined. These will be the active regions of the detectors. Using acetone and propanol the protection polymer is then removed. To passivate the detector area and to create an isolation of the $CoSi_2$ layer, SiO_2 is deposited over the sample by Plasma Enhanced Chemical Deposition (PECVD). Once again using again a photopolymer mask but with a negative lithography process, the silicon oxide on top of the detector which remains unprotected is etched back until the Si cap layer, in the RIE system using CHF_3+CF_4 reactive gas (Fig. 4.7(e)). The protection polymer is then removed in an acetone and propanol bath. After this step, an RCA cleaning process is performed.

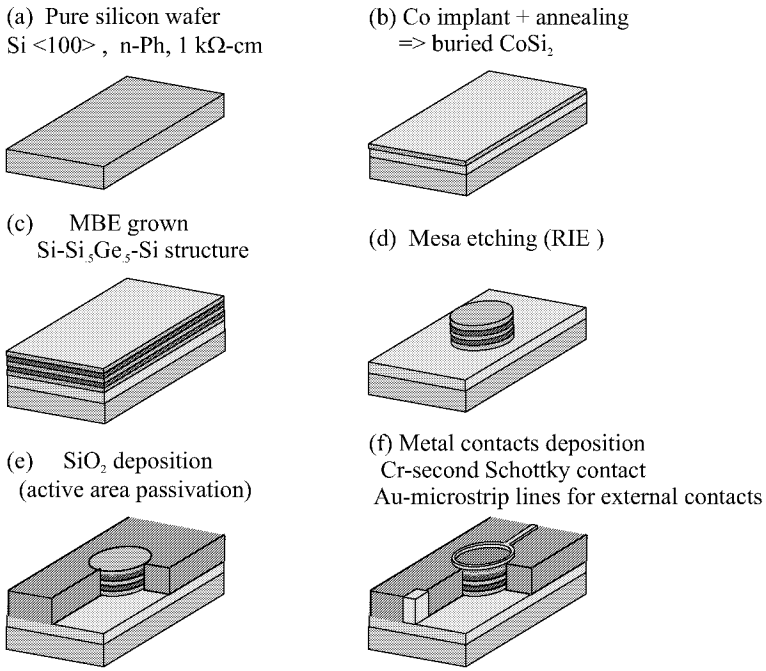

Figure 4.7: The fabrication of vertical Si-SiGe SL detectors.

4.5.2 Metal contact deposition

The contacts between the Si and the metals are very important for the electrical properties of the detector. Impurities or thin SiO_2 at the Si-Metal interface change the Schottky barrier height and increase the recombination at the interface. By controlling the quality of the interface the reproducibility of the Schottky contact is maintained. The top contact is realised by a Lift-Off process. First a polymer mask is defined by a negative lithography process. Immediately after an HF cleaning for 15 s -for removing the SiO_2 formed during the RCA cleaning procedure, the metal is deposited. The metalisation is made in an electron beam evaporator and a semi-transparent film with a thickness of 8-10 nm is deposited. We choose chromium for the top contact, because of its low resistivity Schottky contact formed by it and good adhesion to the SiO_2. Standard lithography and RIE processes are used to open a window in the oxide to form a contact with the buried $CoSi_2$ layer. A lift-off process is used for forming the microstrip lines and the contacting pads of the detectors. Their metallization consists of 20 nm Cr (for improved adhesion) and 200 nm Au. The microstrip lines are 4 mm long for allowing electro-optic measurements free of reflections from their terminations.

4.6 Electrical characterisation of the photodetectors

4.6.1 Current-Voltage dependence

The current - voltage characteristic (I-V curve) contains important information about the detector. From these curves, information about the dark current, effective Schottky barrier heights and the quality of passivation can be extracted. The electrical characterisation of the photodetectors was performed using an HP-semiconductor analyzer. The dark current characteris-

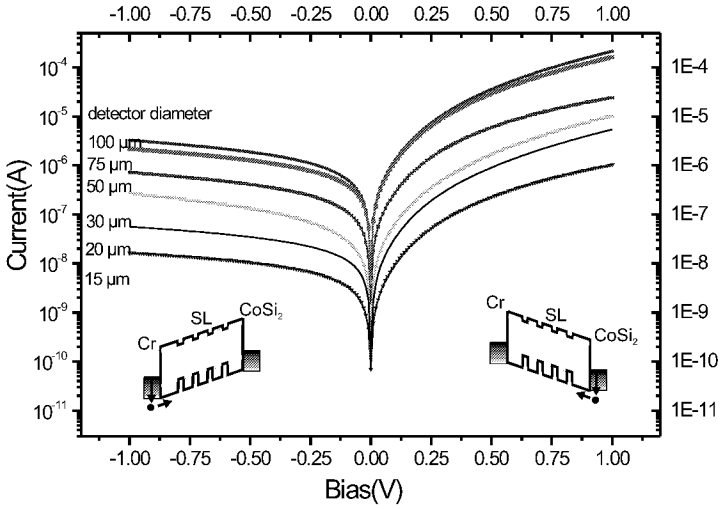

Figure 4.8: Dark current - voltage characteristic for the SL-1 detectors with different mesa diameters. In the inserts the hole transport is sketched in the band diagrams for two bias directions.

tics of the SL-1 detectors with different mesa diameters are shown in Fig. 4.8. Depending on the bias direction, the current is determined by the Schottky contact on the top or the bottom metal contact. Negative voltage here means that the Cr top contact has a negative potential with respect to the $CoSi_2$ contact. Both electrodes form Schottky contacts and since for both contacts, the Schottky barriers for holes are lower than that for electrons [1], the hole current dominates the dark current. The inserted sketches of the en-

ergy band diagrams for the two bias directions illustrate the flow of holes. At higher voltage, when saturation occurs, the current became approximately proportional to the voltage. By extrapolating this part to 0 V and using the Richardson formula for the effective Schottky barrier, Φ_{eff} can be calculated (4.1).

$$\Phi_{eff} = \frac{k_b T}{q} \ln \frac{AA^* T^2}{I_s} \tag{4.1}$$

From the current-voltage characteristics Schottky barrier heights of ϕ_{eff-Cr}= 0.48 eV for the Cr-Si interface is extracted. This value is consistent with data in the literature [1]. For the $CoSi_2$-Si interface values of $\phi_{eff-CoSi_2}$=0.32-0.35 eV were obtained. The Schottky barrier between the $CoSi_2$ and Si is somewhat lower than the expected theoretical value of 0.4 eV, which indicates the existence of imperfections at the interface. This can also be the reason for the higher current at negative bias voltages.

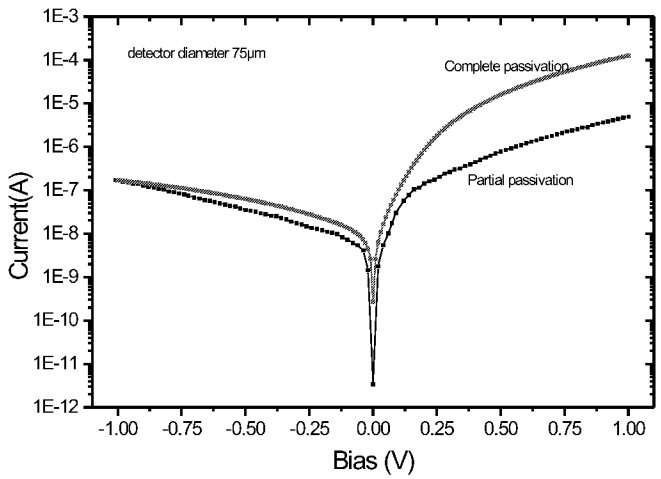

Figure 4.9: Comparison of the dark current-voltage characteristics for a 75 μm diameter detector when a complete or partial passivation of the mesa is performed.

It should also be taken into consideration that for mesa definition part of the sample is etched back till to the $CoSi_2$ layer. The SiO_2 deposition is made in an oxygen atmosphere which will influence the $CoSi_2$ layer and in addition impurities can arrive at the mesa edges inducing a lowering the of $CoSi_2$-Si Schottky barrier. To verify this assumption, we prepared a sample where

only half of the material was etched back, followed by the SiO_2 passivation. A significant decrease of the current on the $CoSi_2$ side of the I-V curve is obtained, while no significant change in the current is observed for the Cr side. Schottky barrier height measurements give now values of $\phi_{eff-CoSi_2} =$ 0.38-0.39 eV for the $CoSi_2$ contact. The I-V characteristics for a detector with a diameter of 75 μm for both structures are compared in Fig. 4.9. The dark current density is 15 mA/cm^2 at a voltage of 1 V. The dark current density was constant for detectors of different area. In Fig.4.10(a) and 4.10(b) the dark current for a SiGe SL at -1V ($CoSi_2$ side) and +1V (Cr side) are plotted as a function of the detectors area. The linearity of the data indicates that currents along the edge of the mesa did not play a significant role. The dark current-voltage characteristic of the SL-2 detector was similar to that shown in Fig. 4.8.

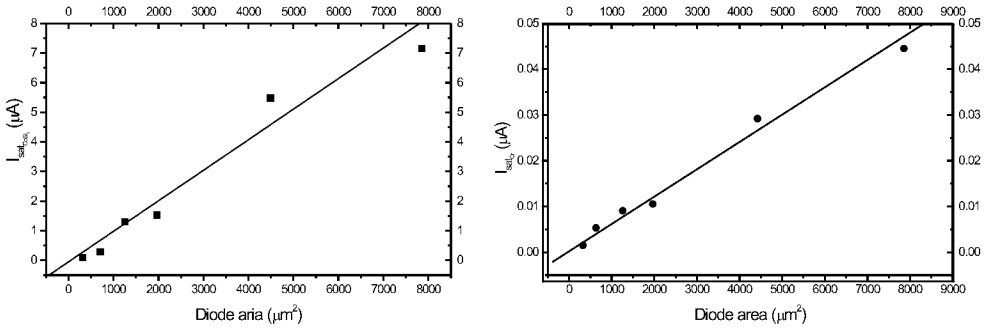

Figure 4.10: The dark current as a function of the diode area. (a) $CoSi_2$ contact,(b) Cr contact.

4.6.2 Photocurrent measurements

By measuring the photocurrent response of the detector by illumination in the absorption range of the active area, the characteristic parameters, responsivity and quantum efficiency, can be calculated. The detectors are illuminated via an optical fiber with a core diameter of 8 μm. In this way, the light is directed exactly onto the detector area. The light sources are InGaAs laser diodes at wavelengths of 1320 nm and 1550 nm. The laser radiation is coupled to the optical fiber and its intensity is measured at the other end with a calibrated photodetector. Using a lock-in technique and a

3D micropositioning stage, the fibre is moved over the detector area to maximize the light coupled to the structure. The detectors is then connected to a HP semiconductor analyzer and the currents under the illumination and non illumination condition are successively measured. The photocurrent is the difference between the current under illumination and the dark current. Fig. 4.11 shows the photocurrent responses of a SL-1 detector (39% Ge) with a diameter of 50 μm at a wavelength of 1320 nm at different light illumination intensities. Fig. 4.12 shows the photocurrent from a SL-2 (45%) detector at a wavelength of 1550 nm. At this wavelengths the silicon is transparent. This means that the photocurrent is the result of the light absorption in the SiGe quantum wells. By photon absorption electron-hole pairs are created in the SiGe layers.

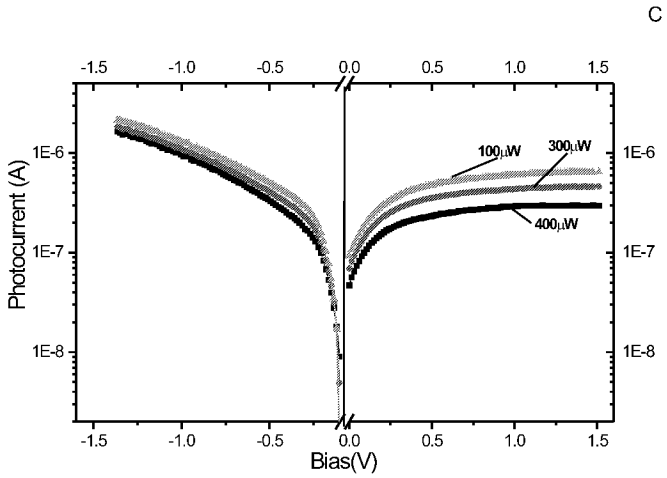

Figure 4.11: The photocurrent response from a SiGe SL detectors with 39% Ge content at a wavelength of 1320 nm.

For the negative bias direction ($CoSi_2$ contact), the photocurrent response saturates for voltages exceeding -0.7 V and its much larger than for positive bias direction (Cr contact). However in negative bias direction the dark current exceeds the photocurrent response by one order of magnitude. In the positive bias direction the photocurrent response is about one order of magnitude higher than the dark current. It was also observed that the photocurrent response increases sublinearly with radiation power. The curves for the SL-1 detector and SL-2 detectors have similar shape, but the photocurrent response is different. From the photocurrent response, we calculated the

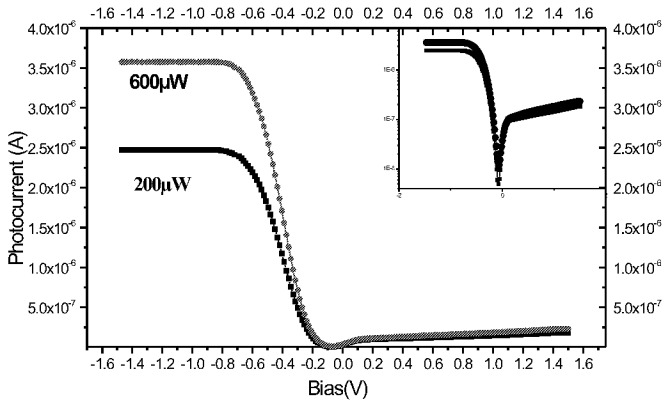

Figure 4.12: The photocurrent response from a SiGe SL detectors with 45% Ge content at a wavelength of 1550 nm. *Log* scale is used in the inset.

responsivity and the overall quantum efficiency of the detectors. The responsivity is obtained by dividing the photocurrent, I_{ph}, by the light intensity, I_0:

$$R(AW^{-1}) = \frac{I_{ph}}{I_0} \tag{4.2}$$

The quantum efficiency is then :

$$\eta = R\frac{h\nu}{e} \tag{4.3}$$

The quantum efficiencies for SL-2 detector are shown in Fig. 4.13 for both 1320 nm and 1550 nm wavelengths. We found maximum values for the quantum efficiency of 5.2% for $\lambda = 1320$ nm and 1% for $\lambda = 1550$ nm. It is easily observed from the graph that the quantum efficiency decreases by increasing the radiation intensity. In table 4.1, the data for the responsivity (in mA/W) and overall quantum efficiency are summarized for the two superlattice detectors and for a double Schottky detector of similar design, but with pure Si instead of the Si/SiGe superlattices between the $CoSi_2$ and Cr contacts. This detector is described in detail in [27]. The detection of this device is based on the creation of holes due to the internal photoeffect at the metal-semiconductor interfaces (see paragraph 2.2.1).

As shown in table 4.1, the detectors with 45% Ge (SL-2) have a 100 times higher quantum efficiency than a similar Si-$CoSi_2$ Schottky barrier detector

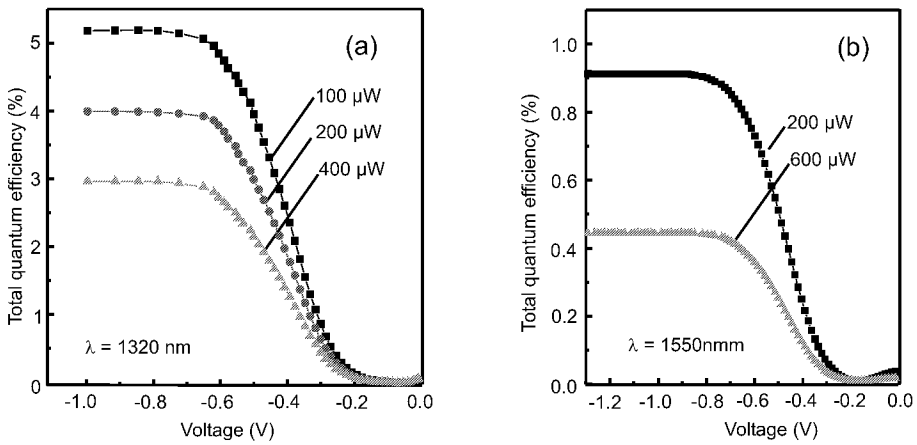

Figure 4.13: Total quantum efficincy of the SL-2 detectors for for $\lambda = 1320$ nm radiation (a), and for $\lambda = 1550$ nm radiation (b). The radiation power is indicated at the curves.

[28]. Obviously, in the SiGe superlattice detector, electron-hole pairs are created in the Ge-rich regions. Our data indicate, that the absorption coefficient at the wavelength of 1300 nm in the Ge-rich regions may approach the absorption coefficient of pure Ge. Furthermore the absorption efficiency of the device is enhanced by multiple reflections, because the semiconductor and the electrodes form an optical cavity (Fig. 4.7). The responsivity of the SL-1 detector is about half the responsivity of the SL-2 detector for $\lambda = 1320$ nm. We attribute this to the reduced absorption in the superlattice with lower Ge content. For $\lambda = 1550$ nm the responsivity of the SL-1 detector is comparable with the Schottky detector. This indicates that the energy

		λ=1320 nm		λ=1550 nm	
		η (%)	R (AW^{-1})	η (%)	R (AW^{-1})
Schottky detector	pos. bias	0.01	0.1	0.005	0.06
	neg. bias	0.03	0.3	0.015	0.18
$Si_{61}Ge_{39}$ SL	pos. bias	0.3	2.9	0.008	0.1
	neg. bias	1.6	17	0.028	0.35
$Si_{55}Ge_{45}$ SL	pos. bias	0.45	4.7	0.08	1
	neg. bias	5.2	55	0.9	12.5

Table 4.1: Efficiency and responsivity comparison of the SL-1, SL-2 and pure Si-Schottky detectors. The Schottky detector is described in detail in [27].

gap in the detectors with 39% Ge in the quantum well is too large for the creation of electron hole pairs by photons of this wavelength. The strong dependence of the dark current on the bias direction can be explained by the different Schottky barrier heights of the contact metals. The dependence of the photocurrent and the quantum efficiency on the bias direction is not clear. We speculate that the Schottky barriers will be influenced by the carrier density in the structure. Furthermore, the energy band alignment studies of the SiGe-Si heterostructure have shown that the change Δ in the bandgap E_g leads to a small offset in the conduction band (10% x Δ) as compared to the offset in the valence band (90% x Δ) [29]. Therefore, electrons move freely across the SiGe-Si interfaces at room temperature ($E_{C,Si}$-$E_{C,SiGe} \approx 25$ meV)), but the holes are mostly trapped in the quantum wells ($E_{V,Si}$-$E_{V,SiGe}$ $\approx$ 300 meV)), see Fig. 4.14.

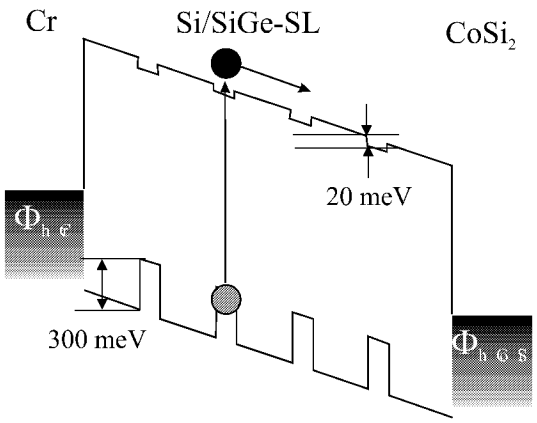

Figure 4.14: Energy band diagram for a SiGe superlattice detector

The density of the photogenerated carriers in the wells remains larger than in the Si regions and recombination takes place in the quantum wells. Although a direct radiative recombination is forbidden in Si, in the undulating SiGe structure, due to the random composition of the alloy, k-vector conservation is relaxed and radiative transitions are allowed. Significant photoluminescence from Ge rich regions at $\lambda = 1550$ nm was measured [21]. Probably the recombination rate in the quantum wells is strongly enhanced as compared to uniform materials. This enables a short electrical response time of the detectors.

4.6.3 Comparison with related results

For the *p-i-n* diode $Si/Si_{0.55}Ge_{0.45}$ superlattice detectors in waveguide geometry, maximum total quantum efficiencies of 11 % have been reported for $\lambda = 1300$ nm [16]. The length of these waveguides was several mm, therefore much higher absorption can be expected, as compared to normal incidence detectors. Normal incidence $Si/Si_{0.5}Ge_{0.5}$ superlattice detectors, also fabricated as pin diodes, showed 1 % total quantum efficiency for $\lambda = 1300$ nm [17]. For this detector the dark current density was 60 mA/cm^{-2}. The results for the SL-2 detector operated with a positive bias voltage (0.45 % total quantum efficiency, 15 mA/cm^{-2}) are comparable with these numbers. For negative bias our detector is more sensitive, but also has a much larger dark current density. Recently, detection of radiation for $\lambda = 1550$ nm has been reported using a 240 μm long $Si/Si_{0.5}Ge_{0.5}$ superlattice MSM detector [30]. For this experiment an internal responsivity of 0.1 A/W has been reported. Considering the thin structure and the correspondingly short absorption length of our detectors, our results on the quantum efficiencies are very satisfying. In addition, the quantum efficiency measured at a wavelength of 1550 nm represents the highest total quantum efficiency reported for a vertical detectors using SiGe quantum wells.

4.7 Electrical time response measurements

After the analysis of the static electrical behavior of the detectors, their dynamical characterization will be presented in the following subsections. The diodes are illuminated with an ultra-fast laser pulse and their electrical response is analyzed via an electro-optic sampling method (see Chapter 3). The characterization is performed at the wavelengths of 1300 nm and 1550 nm where the SiGe SL is active, and also at 800 nm where Si is an optical absorber, for the purpose of comparison with a pure Si detector with the same geometry.

4.7.1 Geometrical limits of the electrical response time

The response of a diode for a short light pulse excitation is defined by two parameters:

- the drift time of the carriers to the electrodes
- the RC time constant of the detector

After light excitation the created photo-carriers move to the contacts, under the influence of the electrical field existing in the structure, giving rise to an electrical current $I_c(t)$. This current depends only on the carrier dynamics. In silicon at a high enough electrical fields (E>10^4 V/cm), the carriers move towards the contacts with a constant saturation drift velocity, which for Si is $1{\cdot}10^7$ cm/s for both electrons and holes. The minimum transit time is then:

$$t_{tr} = \frac{1}{2} \cdot \frac{d}{v_s} \tag{4.4}$$

where d is the interelectrode distance and v_s is the saturation drift velocity. The vertical MSM design is similar to a planar capacitor. In combination with the metallic conduction lines for integration the active area with the external circuit, the RC time constant of the device is defined:

$$t_{RC} = R_l \cdot \epsilon_0 \cdot \epsilon_r \frac{A}{d} \tag{4.5}$$

where R_l is the microstrip line resistance, A is the diode area and d the interelectrodes distance. The RC time constant defines the response speed of the device $h(t)$ and is independent of the carrier dynamics in the active area of the detector. The total electrical time response of the diode is a convolution of the carrier current and the circuit response, eq. 4.6:

$$i(t) = i_c(t) \otimes h(t) \tag{4.6}$$

We can see from eq. 4.5 that a small detector area is desirable for a fast detector. Further, a small interelectrode distance will give a short transit time for the carriers (eq. 4.4), but in this case the RC time constant will increase. An ideal diode will have a RC time constant much smaller than the transit time. In this case, the detector response will reflect the carriers dynamics in the structure. In our design the resistance of the microstrip line is 10-15 Ω. The RC time constant varies between 2.4 ps for a small detector to 20 ps for a detector with a diameter of 100 μm. Comparing these times with the carrier transit time of 2.3 ps, it appears that the response for these detectors will be limited by the RC time constant of the device. In the following part we will analyze the response time only for detectors with a RC time constant closer to the transit time of the carriers.

4.7.2 Time response measurements in the IR wavelength range

The temporal response of the photodiodes is measured by an optical pump-probe technique (see chapter 3). The photo-excited carriers in the detector

under investigation give rise to an electrical pulse traveling along the microstrip transmission line. The sampling electro-optical crystal is placed as close as possible to the active area to avoid pulse dispersion in the microstrip line.

Figure 4.15 shows the fast response of a detector with 39 at% Ge and a sensitive area of 710 μm^2, measured at a pump wavelength of 1300 nm. A full width at half maximum (FWHM) of 11.6 ps was measured for the electrical pulse response. Due to the fact that SL-1 detectors showed no absorbtion at a wavelength of 1550 nm, at this wavelength, the electrical time response was measured for SL-2 detectors. The response from a detector with the same area (700 μm^2) is shown in Fig. 4.16. In this case a FWHM of 9.4 ps is obtained. The difference in response time from the two detectors is due to a smaller Si cap layer in the SL-2 detectors, resulting in a shorter transit time for the carriers. The corresponding -3dB bandwidth amounts to f_{3dB} = 17 GHz. All the above measurements were performed at 300 K.

The response times presented in Fig. 4.15 and 4.16 represent, to our knowledge, the fastest responses to infrared radiation obtained from a SiGe detector. As shown in Fig. 4.17 (a-b), we compare the response of a SL-1 detector at the wavelength of λ=1300 nm with the response at the wavelength of λ=800 nm. As we can see, there is no difference in the detector time response, except for the signal amplitudes which are determined by light absorption at this wavelength. For a better comparison, we have studied a series of different MSM detectors of different size, made from pure Si. This allows the separation of the contribution of carrier drift and RC time constants in the observed device response speed. The smallest device (80 μm^2) is the fastest, with a total response time of 3.2 ps FWHM [27]. This response is determined by the drift time of the photogenerated carriers, which are accelerated to saturation drift velocity ($\sim 10^7$ cm/s). The larger devices with areas up to 4000 μm^2 show increasing contributions from the electrical RC time constants, which increase the total response time. As shown in Fig. 4.17(a) and (c), we compare the response of a SL-1 detector to the response of a pure Si MSM detector which has the same area and thickness.

The observed electrical signal f(t) can be described by three exponential functions [31]:

$$f(t) = a \cdot [1 - \exp(-t/\tau_1)][\exp(-t/\tau_2) + b \cdot \exp(-t/\tau_3)] \qquad (4.7)$$

The first factor represents the rising part of the signal, characterized by a time constant τ_1. The decay of the signal is composed by the sum of two exponential functions with time constants τ_2 and τ_3. The analysis yields values of τ_1 = 3 ps, τ_2 = 3.8 ps and τ_3 = 70 ps, for the SiGe SL detector

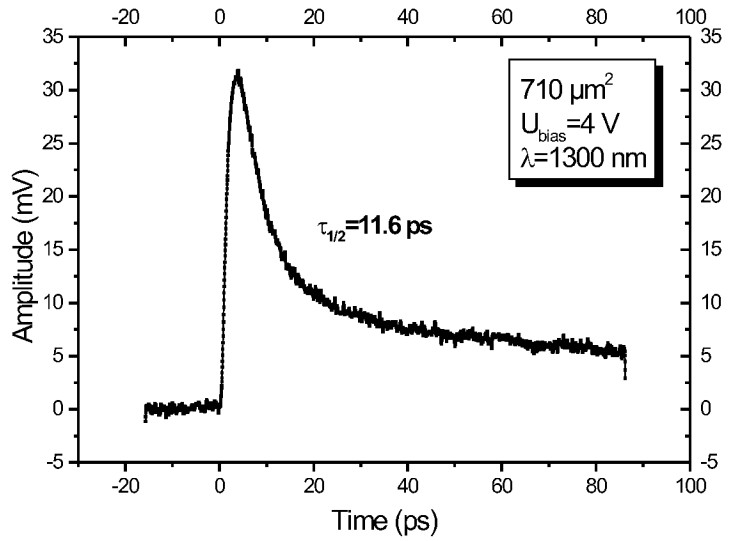

Figure 4.15: Electrical time response from a 39 % Ge content SiGe superlattice detector at a wavelength of 1300nm.

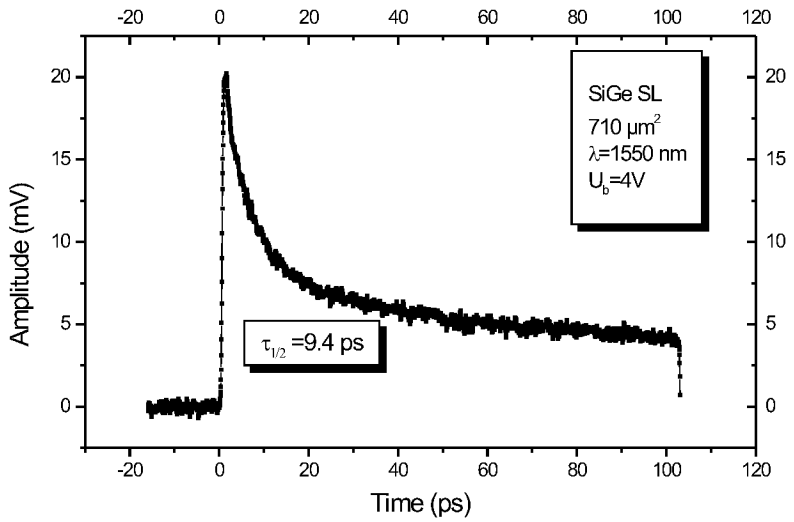

Figure 4.16: Electrical time response from a 45 % Ge content SiGe superlattice detector at a wavelength of 1550nm.

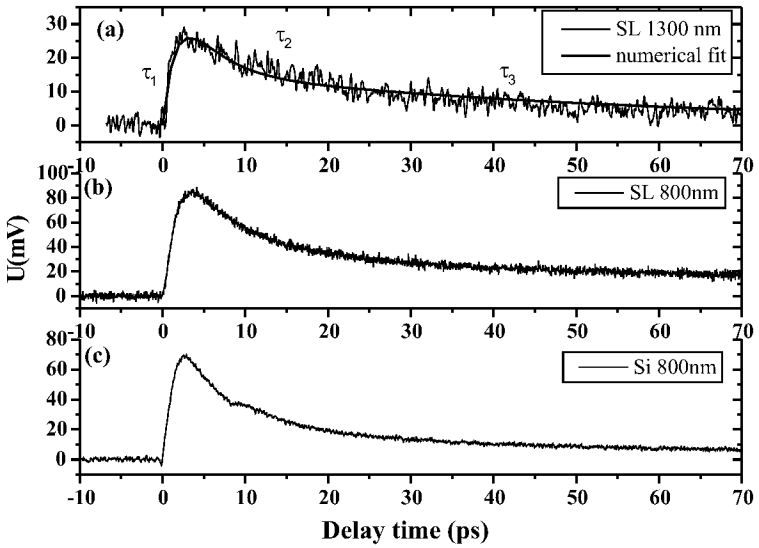

Figure 4.17: Electrical time response from a 39 at% SiGe SL detector at λ= 1300 nm (a); λ= 800 nm (b) and a pure Si MSM detector at λ= 800 nm (c).

with 39 at% Ge. This may be compared to the response of a pure Si detector (τ_1 = 2.9 ps, τ_2 = 3 ps). The total current of the detectors is given by the contribution of the electrons and holes, which are accelerated by the homogeneous applied field. The duration of the internal current is equal to the electron or hole transit time to the electrodes. In an ideal circuit, the rise time of the signal (τ_1) is extremely fast. In the experiment it is given by the RC_{ext} time constant of the external circuit, but not influenced by the detector capacity C_{det}. Therefore, the parameter τ_1 gives no information about the carrier dynamics. Due to the higher drift velocity of the electrons in comparison with that of the holes, the total response is characterized by a fast component τ_2, reflecting the rapid sweep-out of the electrons and a slower component τ_3, which is due to the holes. Comparing τ_2 in Si (3 ps) and SiGe SL (3.8 ps), we conclude a lower speed of the electrons in SiGe. This is due to a reduced mean free path between the SiGe quantum wells. In Fig. 4.18, a comparison of the normalized signals from SiGe SL detector and a pure Si MSM detectors, measured at room temperature for a detectors with an area of 710 μm^2 is shown. As we can see, after a delay time of 90 ps, the signal has decreased to 17 % of its maximum value for the SiGe detectors and 9 % for the pure Si one. This indicates a considerable density of traps in the detector structure. It is known, that Si on top of a buried $CoSi_2$ layer

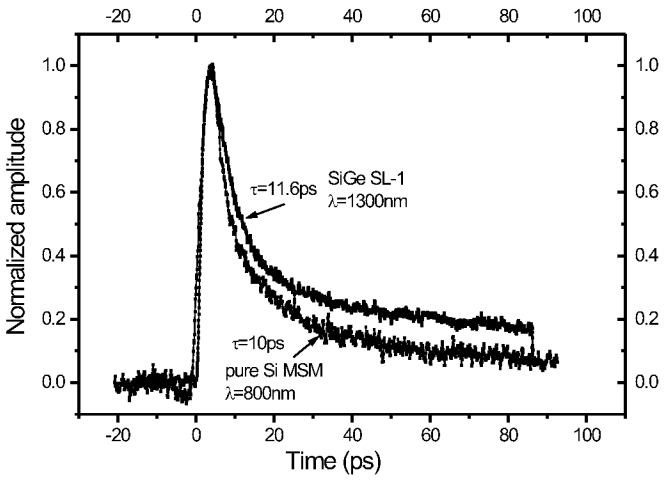

Figure 4.18: Comparison of the normalized signal from SiGe SL detector at λ= 1300 and a pure Si MSM detector at λ= 800nm. Detector area 710 μm^2.

contains a high density of misfits dislocations. These and other defects may act as traps for the photo-generated charge carriers. If a large density of traps is rather shallow, thermally activated hopping transport is possible. Carrier escape from the traps is then expected to be responsible for the delayed current long after the excitation [32]. A difference in the amplitude tail is expected between SiGe and Si detectors, taking into consideration the misfit dislocations at the interface Si-SiGe layers.

4.7.3 Influence of the applied bias voltage

The electrical time response from a SiGe SL-1 detector at a wavelength of λ=1300 nm as a function of applied voltage is shown in Fig 4.19. A positive voltage was applied to the Cr contact. Due to the different Schottky barriers for the Cr and $CoSi_2$ small built-in electrical field is present in the structure even at 0 V applied voltage. The created photo-carriers are separated by the electrical field and move to the electrodes. The FWHM in this case is 57 ps (see Fig. 4.20). By increasing the applied bias to 3-4 V the signal became stronger and shorter. With increasing electrical field strength, the carriers gain higher drift velocity and therefore, the transit time is reduced. At 4 V the carriers reach the saturation drift velocity and further increase of the field does not change the detector response. The measured FWHM is

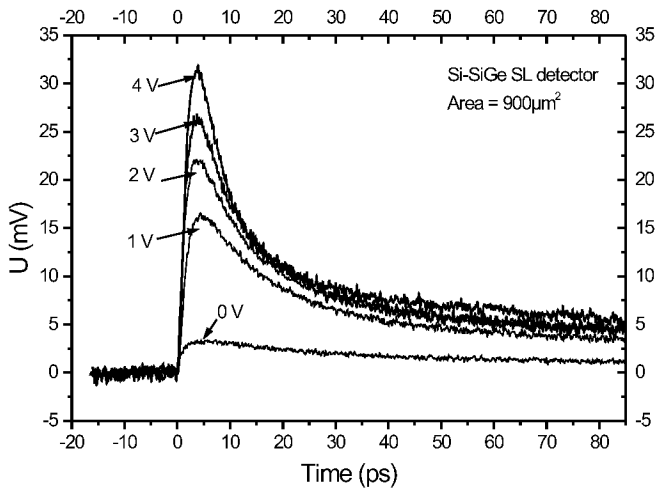

Figure 4.19: Electrical time response from a SiGe superlattice detector as a function of applied bias.

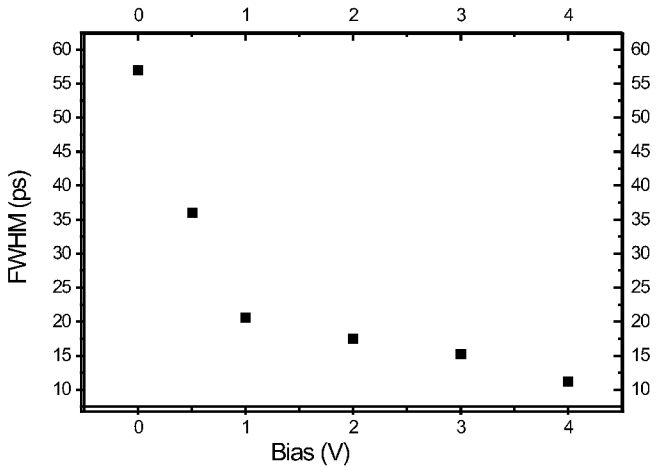

Figure 4.20: Measured full width half maximum (FWHM) from a SiGe superlattice detectors with an area of 710 μm^2 as a functin of applied bias.

presented in Fig. 4.20.

4.8 Conclusion

We have evaluated the performance of vertical metal -semiconductor- metal photodetectors based on SiGe and a buried $CoSi_2$ layer. The details of the ion implantation and molecular beam epitaxy techniques used for the fabrication of vertical MSM photodetectors based on undulating SiGe superlattice structures were presented and discussed. The importance of this geometry for introducing higher concentrations of Ge, for the purpose of bandgap tuning, was also highlighted therein. These devices were of a plate capacitor design with a buried epitaxial $CoSi_2$ layer as the bottom electrode. Since the absorption characteristics of SiGe superlattices have a strict dependence on the Ge concentration, layer thickness and internal stresses, the incorporation of very high concentrations of Ge with minimal interfacial stress and threading dislocations is crucial to obtain high quality devices. it was shown through channelling and electron microscopy measurements that the interfaces were largely free of threading dislocations. The back scattering yield obtained for the undulating SiGe superlattices was only 6%, thereby certifying the interface quality. These observations were also borne out by the static electro-optic properties analyzed via current-voltage characteristics. The critical influence of the Clean Room structuring processes on the Schottky barrier height and dark current of the device was also reiterated. Our measurements performed on devices with different Ge concentration have demonstrated, once more, the critical importance of the Ge concentration for obtaining bandgap energies under 0.8 eV. Total quantum efficiencies as high as 5.2 % for $\lambda = 1320$ nm and 0.9 % for $\lambda = 1550$ nm were measured for a detector with 45 at.% Ge. For 39 at.% Ge, we obtained values of 1.6 % and 0.03 % respectively. The sensitivity of the device is enhanced by the optical cavity like design but suffers from the small thickness of the active area. The dark current density was determined to be 15 mA/cm^2, which is comparable to the dark current density of similar devices. The typical excitation pulse length in the pulse excitation spectroscopy was 150 fs. For a diode with an electrode distance of 400 nm and an area of 710 μm^2 a record electrical time response of 11.6 ps was measured. The excitation wavelength was $\lambda = 1320$ nm. The detectors with 45 % Ge content have a smaller inter-electrode distance of 330 nm. The electrical time response of 9.4 ps at a wavelength of $\lambda = 1550$ nm was measured. The plate capacitor design has the disadvantage of high RC time constant. This dominates the response time for bigger area detectors and limits the inter-electrode distance.

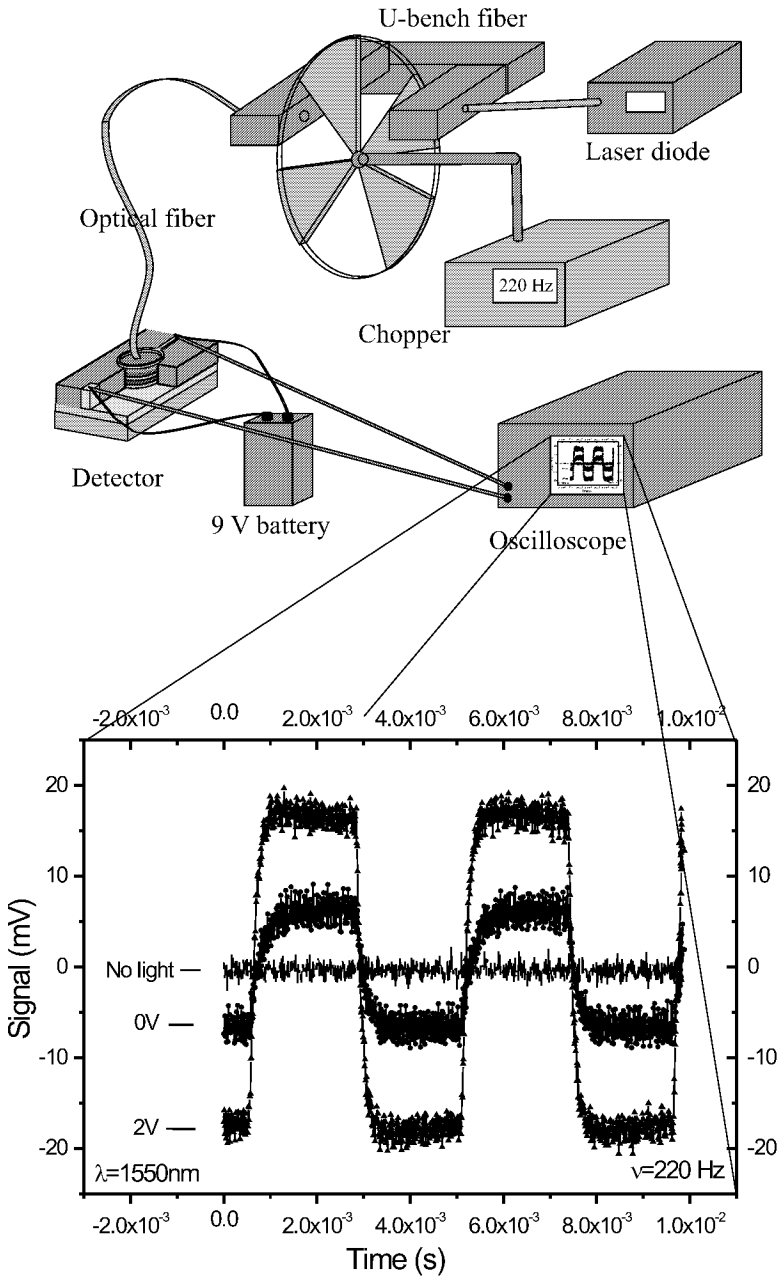

Figure 4.21: Oscilloscope signal given by a SiGe SL detector. Modulation freqency 220 Hz.

A comparison of the our SiGe detectors with pure Si devices with the same design parameters was also presented. It was shown that vertical SiGe detectors in the infrared range possess the same high-speed properties as pure Si detectors in the visible region.
In order to demonstrate the usefulness of our device, we performed the following basic experiment. We used a 9 V battery for biasing the detector. The detector's signal was directly sent to an oscilloscope without any amplification. Because the laser diode was a continuous wave one, we used an U-bench fiber connector and a chopper for light modulation. The signal measured by the oscilloscope is presented in Fig. 4.21. The light intensity is 400 μW at a wavelength of 1550 nm and the light frequency modulation is 220 Hz.
Despite the clear output signal, at present, the detector still suffers from a relatively high dark current and a certain density of process-induced defects which limit both the sensitivity and the room temperature speed (long decay tail). We believe that these limitations can be overcome by finding a way for a better passivation of the detector mesa and by making Si-$CoSi_2$ wafers with a defect free silicon top layer available.

Chapter 5

Metal - Germanium - Metal detectors

5.1 Introduction

Most silicon-based photodetectors make use of the band-to-band absorption, where an electron is scattered from the valence band into the conduction band by an incident photon. Figure 5.1 shows the variation of the optical absorption coefficient with wavelength for several semiconductor materials [1]. A comparison between the absorption curves of indirect and direct band gap semiconductors reveals a striking difference. Direct band gap semiconductors show a step like onset of the band to band absorption as soon as the photon energy $h\nu$ exceeds the gap energy E_g, whereas the the indirect ones do not. This difference is a consequence of momentum conservation, implying that only vertical transitions are allowed in the k-space. Because of this constraint optical transitions, both emission and absorption, are strong in direct semiconductors. The absorption coefficient may attain values above 10^4 cm^{-1}. The transition from indirect to direct behavior can be nicely seen for Ge. Ge has an indirect gap value of 0.66 eV. In spite of that its absorption is quickly dominated by direct transitions, since the direct gap of Ge of 0.86 eV is only slight larger. Therefore, pure Ge is well suited as an absorbing material for photodetectors in the near-infrared up to 1550 nm. There exist numerous detector concepts in order to fulfill the different requirements of specific applications ranging from high detectivity to ultra-fast response and high resolution arrays. Fast MSM photodetectors fall into two categories: fast response due to enhanced carrier recombination (short carrier lifetimes) or fast carrier collection due to a short transit time to the electrodes. In the first case, the semiconductor is heavily damaged or doped to obtain a

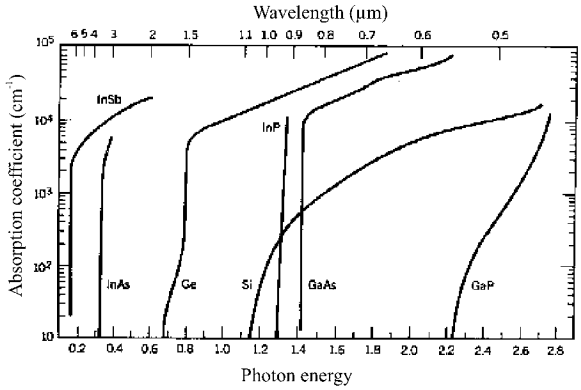

Figure 5.1: Absorption coefficient as a function of wavelength for various semiconductors.

high density of recombination centers, but strongly doped or even disordered material limits the carrier mobility and lowers the quantum efficiency. The MSM interdigitated design is easily adapted to these devices. Previous work has focused mainly on GaAs and InGaAs heterostructures [33, 34], only very few reports are available for crystalline Si [35] or Ge [36]. However, the development of epitaxial cobalt disilicide and its compatibility with crystalline Si permitted the change from the interdigitated electrodes to a vertical plate capacitor design with submicrometer drift lengths and optimum carrier saturation mobility [37]. At present, the fastest electrical response from a MSM detector based on crystalline Si is 14 ps for the interdigitated electrode design [35], but 3.2 ps for the vertical plate capacitor geometry [38]. Due to the use of crystalline Si, these detectors work well at $\lambda = 1.1$ μm, but the quantum efficiency drops quickly at longer wavelengths. For IR absorption at $\lambda = 1.5$ μm pure crystalline Ge is a suitable material. The epitaxial growth of high quality Ge on Si has been demonstrated before. Recently good quality Ge films on Si(111) were grown by chemical vapor deposition (CVD) using a low temperature deposited Ge buffer layer [39], and surfactant mediated epitaxy (SME) [40]. Due to the lattice mismatch between Si and Ge, the growth of Ge on Si rapidly leads to island formation (Stransky-Krastanov growth mode with a critical thickness of about 1 nm). Thicker films relax by the formation of a dislocation network with defect densities of up to 10^{12} cm^{-2} [41]. It has been shown that on Si (111), the island formation can be suppressed by using Sb as a surfactant. During the MBE process, Sb gravitates onto the surface and reduces the mobility of the Ge atoms [42]. In Chapter 4 vertical MSM detectors using epitaxial $CoSi_2$ buried metal electrodes were

demonstrated. Using Si-SiGe layers as the photosensitive material, the heterostructure Cr/Si-SiGe-Si/$CoSi_2$ showed excellent performance in ultrafast MSM devices. It was then attempted to replace the Si-SiGe layer by a Ge thin film. Therefore Ge was grown on top of the $CoSi_2$ layer using the SME technique explained in the following paragraph and good crystalline quality was achieved [43]. Nevertheless, the MSM plate capacitor detectors with Ge as the intended active layer suffered from additional problems during Ge epitaxy on $CoSi_2$ and good Schottky barriers with low dark currents could not be obtained. In this chapter the fabrication of devices using good crystalline quality epitaxial Ge films integrated on silicon is demonstrated.

5.2 Growth of Ge/Si(111) heterostructures

High resistivity Si(111) wafers ($\rho > 1000\ \Omega$·cm) were prepared by a standard RCA cleaning procedure, omitting the final HF-dip. The wafers were loaded into a MBE chamber with a base pressure of $2{\cdot}10^{-11}$ mbar. The oxide formed by the last cleaning step was removed by heating the wafers to 800 °C for 30 min while providing a small flux of Si. Subsequently a 50 nm thick Si buffer layer was grown at a substrate temperature of 650 °C.

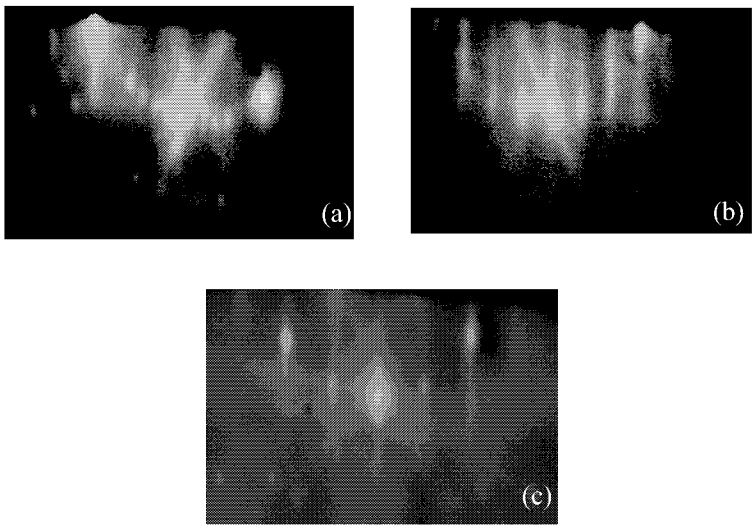

Figure 5.2: RHEED patterns after different process steps. Si(111) with a 7 x 7 reconstruction after buffer growth (a), $\sqrt{3}$ x $\sqrt{3}R30°$ reconstructed surface after coverage with an Sb monolayer (b) and 2 x 1 reconstructed Sb terminated Ge surface after Ge film deposition (c).

The reflection high energy electron diffraction (RHEED) pattern was spotlike and contained reflections corresponding to a 7 x 7 reconstructed surface (Fig. 5.2(a)).

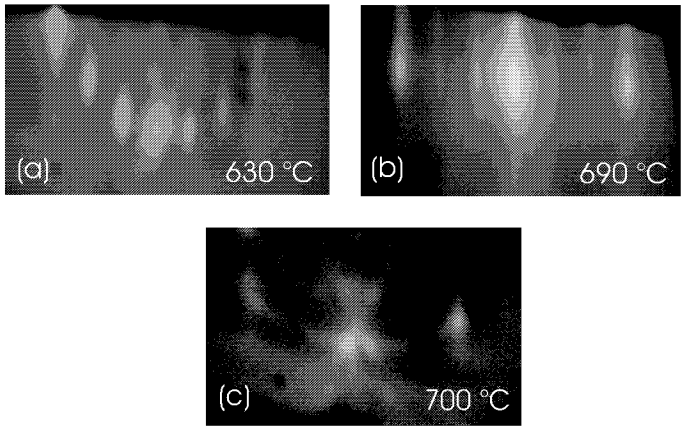

Figure 5.3: RHEED patters indicating the different Sb coverage of the Si (111) surface at different substrate temperatures.

Subsequently, the surface was covered with a monolayer of Sb, which was confirmed by the presence of a $\sqrt{3}$ x $\sqrt{3}R30°$ reconstruction (Fig. 5.2(b)). Finally, a 300 nm thick Ge layer was grown with a Ge deposition rate of 70 pm/s while additional Sb was provided. The spotlike 2 x 1 reconstructed RHEED pattern of the germanium layer after the deposition indicated a flat, Sb terminated surface (Fig. 5.2(c)). Samples were grown at various substrate temperatures in the range from 600 °C to 710 °C. At higher temperatures, it was increasingly difficult to achieve a sufficient Sb coverage for the Si surface, due to the enhanced desorption of Sb. The RHEED patterns depicted in Fig. 5.3 illustrate this observation. In Fig. 5.3(a) spotlike strong reflections from the $\sqrt{3}$ x $\sqrt{3}R30°$ reconstruction indicate a full Sb coverage of the Si surface with Sb at a temperature of 630 °C. The weaker streaklike peaks depicted in Fig. 5.3(b) indicate only partial Sb coverage at 690 °C. For 700 °C, no $\sqrt{3}$ x $\sqrt{3}R30°$ reconstruction was observed. However, the presence of Sb on the surface inhibited the formation of a 7 x 7 reconstruction surface of Si. The Sb cell temperature was regulated at 300 °C, which corresponds to a deposition rate of 0.1 pm/s onto substrates held at room temperature (no Sb desorption expected). The Sb coverage corresponding to the RHEED pattern in Fig. 5.3(b) and 5.3(c) were not sufficient for the desired SME growth of the Ge. In order to form proper Schottky contacts between Ge and Cr, the Sb doping of the Ge film has to be minimized. It has been shown that by increasing

the substrate temperature, Sb segregation is strongly enhanced and therefore the Sb doping reduced [44]. We found that depositing a Sb monolayer first at 600 °C and then raising the temperature was instrumental for obtaining a sufficient Sb coverage for SME growth even at 710 °C.

5.3 Germanium film characterization

In Fig. 5.4 a cross sectional transmission electron bright field micrograph (TEM) of a Ge film grown on Si(111) substrate at 700 °C is shown. Stress induced contrast is visible at the Si-Ge interface, where the mismatch induced stress is relieved by a dislocation network. The interface is smooth. In the left part of the image a threading dislocation can be seen.

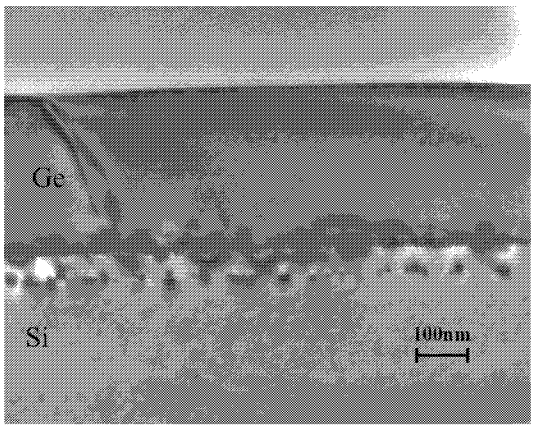

Figure 5.4: Cross-section transmission electron bright field micrograph of a Ge film grown at 700 °C by surfactant mediated epitaxy using Sb.

From the plane view TEM pictures a threading dislocation density of 10^8-10^9 cm^{-2} was measured. The crystalline quality of the films was further studied by Rutherford backscattering spectrometry /channeling (RBS/C).
For all substrate temperatures minimum yields of 5 % for axial channeling and 22 % for planar channeling were found. A typical spectrum is depicted in Fig. 5.5. Good channeling is observed in the Ge film while strong dechanneling occurs at the Ge/Si interface due to the dislocation network. Atomic force microscopy (AFM) measurements confirmed that the surface of the films was flat. A typical RMS roughness of our layers is 0.8 nm. Electrical transport measurements were performed at room temperature in the van der Pauw geometry. We found an increase in the specific resistivity over more

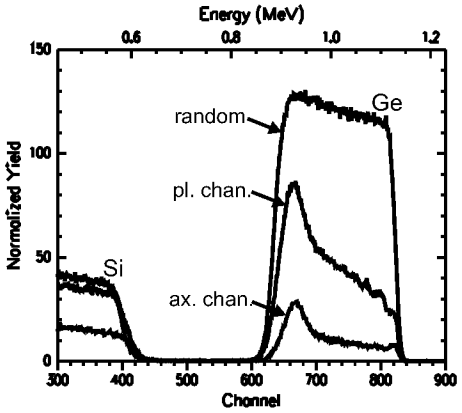

Figure 5.5: Rutherford backscattering and channeling spectra of the Ge film grown at 700 °C. The spectra were measured with He+ ions of 1.4 MeV under normal incidence and a backscattering angle of 170°.

than three orders of magnitude when the growth temperature was increased from 600 °C to 710 °C. This reflects the lower dopant concentration in the films due to the enhanced Sb segregation at higher temperature. Secondary ion mass spectroscopy (SIMS) yielded values for Sb concentration of 10^{18} cm^{-3} for the sample grown at 600 °C and of 4 x 10^{16} cm^{-3} for the sample grown at 700 °C. Samples grown at 700 °C were further process to fabricate metal- germanium- metal (MGeM) photodetectors.

5.4 Device fabrication

The interdigitated design chosen for the MGeM photodetectors is schematically shown in Fig. 5.6.

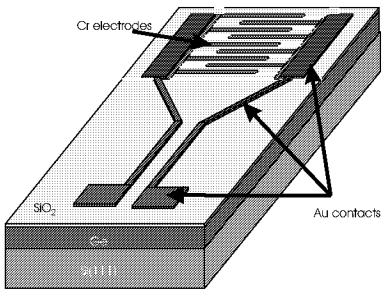

Figure 5.6: MGeM detector design.

After the MBE growth of the germanium film the wafers were cut in 10 x 10 nm pieces for further processing. Prior to cutting the wafer was protected with a thin polymer layer for avoiding surface contamination. After removing the polymer in an acetone and propanol bath the top 30 nm of germanium film were etched off to remove a remaining antimony contamination from the surface. This is expect to reduce the dark current of the future detectors. The solution for removing the Sb layer from the Ge is (CH_3COOH : H_2O_2 : HF) : H_2O with the ratios (3 : 2 : 1) : 10. The electrode deposition and patterning is presented in Fig. 5.7.

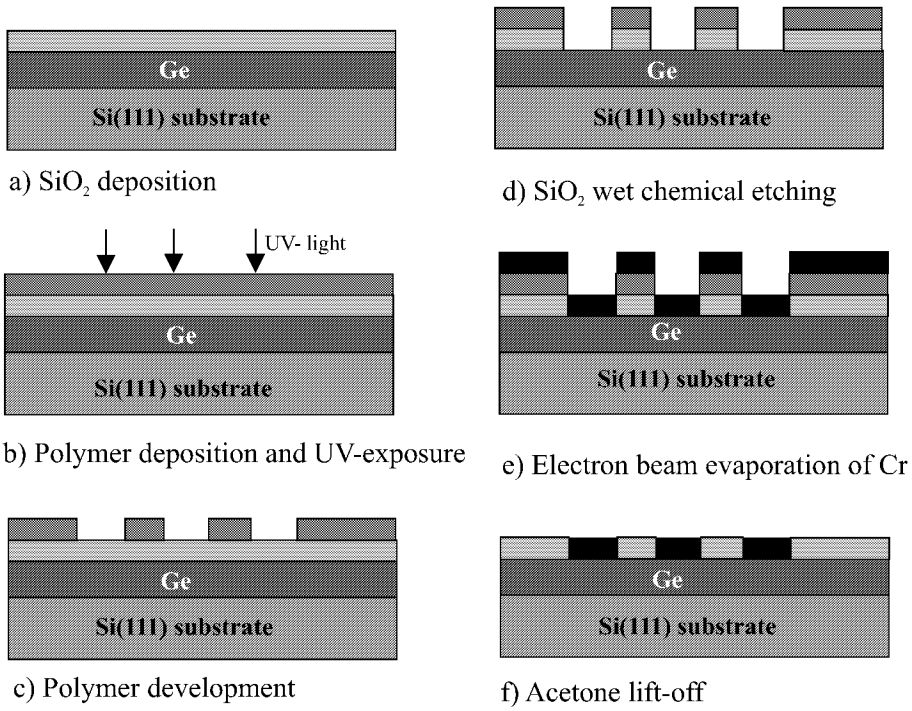

Figure 5.7: Basic steps in finger electrode fabrication.

Subsequently the Ge surface was passivated by depositing 50 nm of SiO_2 by Plasma Enhanced Chemical Vapour Deposition (PECVD). The passivation further reduces the device leakage current (see Fig 5.8). The sample was then covered with a polymer 5206 with a layer thickness of about 500 nm. Using standard negative photolithography process the electrodes form is defined on the polymer mask. By a wet chemical etching process in a AF 91 solution, a window in the oxide layer was opened till to the germanium layer. Immediately after etching 50 nm of Cr was deposited for forming the Schottky

contacts in an Electron Beam Evaporation chamber. The same procedure except the oxide etching is repeted for depositing the electrical contacts (the coplanar lines and the bond pads). The coplanar line are 7 mm long and consist of 20 nm Cr -for increasing the adhesion with the oxide layer- and 200 nm Au. The interdigitated detector area has a quadratic size ranging from 10 x 10 μm^2 to 100 x 100 μm^2, with fingers of 1.5, 2, 3 and 5 μm width and equal separation.
In the following part of the chapter for a easy presentation, the electrode geometry will be expressed only by the electrode spacing, the electrode width always being equal to the electrode separation.

5.5 Electrical characterization of photodetectors

5.5.1 Detector parameters

For electrical measurements, aluminium wires with 50 μm diameter are used to connect the detectors with the measurement set-up. The capacitance of the interdigitated electrode structure can be calculated with the formula [34]:

$$C = \frac{\epsilon_0 \cdot (1 + \epsilon_r) \cdot A}{(l_w + l_a)} \cdot \frac{K(k)}{K(k')} \tag{5.1}$$

where ϵ_0 and ϵ_r are permitivity of vacuum and relative permitivity of semiconductor material, A is active area of the MSM structure, l_a is a distance between fingers and l_w is width of a fingers. The function K(k) and K(k') are complete elliptic integrals:

$$K(k) = \int_0^{\pi/2} \left[\frac{1}{\sqrt{1 - k^2 \cdot \sin^2 \varphi}} \right] d\varphi \tag{5.2}$$

k and k' are expressed by:

$$k = \tan^2 \frac{\pi \cdot l_w}{4 \cdot (l_a + l_w)} \qquad \text{and} \qquad k' = \sqrt{k^2 - 1} \tag{5.3}$$

The capacitance calculation yield values in the range of 1 to 10 fF, depending on the finger separation and width. The calculated coplanar line wave impedance is 60 Ω.

5.5.2 Influence of the fabrication processes on the current-voltage characteristic

The dark current-voltage characteristics are measured using a Hewlett Packard HP 4155 semiconductor analyzer. Due to the symmetry of the structure, (using the same metal for electrodes) only one bias direction will be presented in the I-V characteristics. In the detector region, the oxide deposition passivates the germanium surface and reduces the surface current. This is shown by dark current measurements on a large detector (100 x 100 μm^2, 3 μm spacing) with and without SiO_2 passivation (Fig. 5.8). The passivation im-

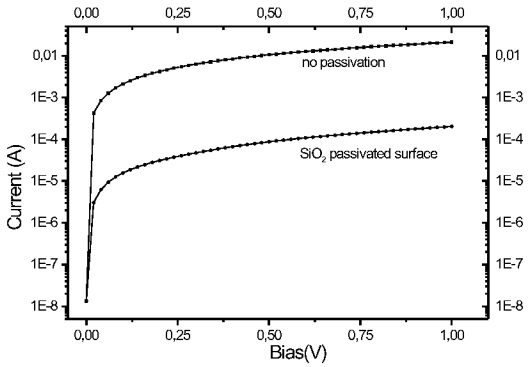

Figure 5.8: The dark current-voltage characteristics of a MGeM detector with and without SiO_2 passivation.

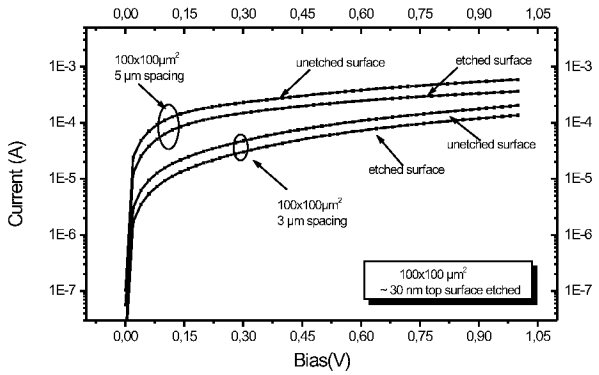

Figure 5.9: The dark current reduced by top 30 nm Ge etching.

proves the dark current by two orders of magnitude. In Fig. 5.9 the decrease of the dark current by etching of 30 nm top Ge surface is shown for detectors with the same area (100 x 100 μm^2) and a spacing of 3 μm and 5 μm.

5.5.3 Photo-electrical measurements

Two laser diodes at 1320 nm and 1550 nm were used as light sources for the DC photocurrent measurements. Light from the optical fiber at vertical incidence is coupled into the detectors by a micropositioning stage.

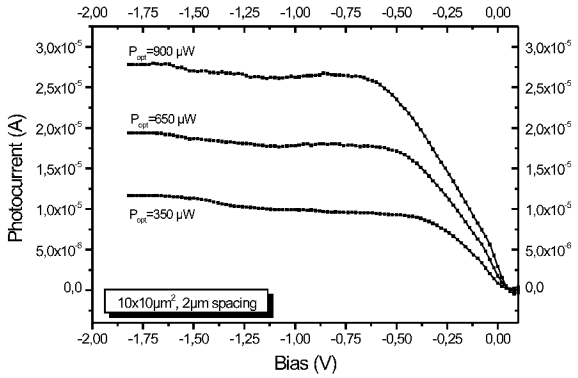

Figure 5.10: The measured photocurrent from a MGeM detector with an area of 10x10 μm^2 and 1.5 μm finger spacing at different optical power intensities.

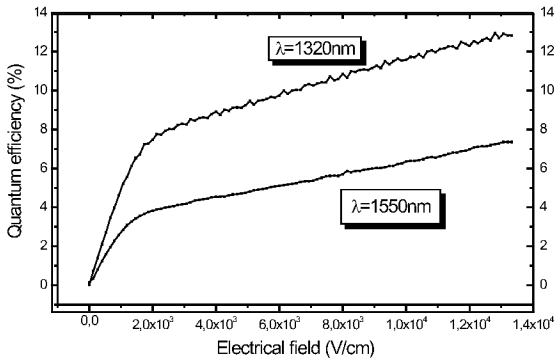

Figure 5.11: Total external quantum efficiency at λ = 1320 nm and 1550 nm versus electrical field strength for a detector with an area of 100 μm^2 and 1.5 μm electrode spacing.

Fig. 5.10 shows the photocurrent response from a detectors with a 100 μm^2 area and 2 μm electrode spacing at a wavelength of 1550 nm for different optical excitation intensities. As can be seen in the figure the photocurrent increases linearly with the radiation intensities. This linearity is maintained for optical input powers from 100 μW to 1 mW. The total external quantum efficiency at wavelengths of 1320 nm and 1550 nm versus electrical field strength for a detector with an area of 100 μm^2 and 1.5 μm electrode spacing is presented in Fig. 5.11. The photoresponse increases rapidly, if an electrical field is applied. For fields exceeding $1.3 \cdot 10^4$ V/cm overall quantum efficiencies of 13 % at a wavelength of $\lambda = 1320$ nm and 7.5 % at $\lambda = 1550$ nm were measured.

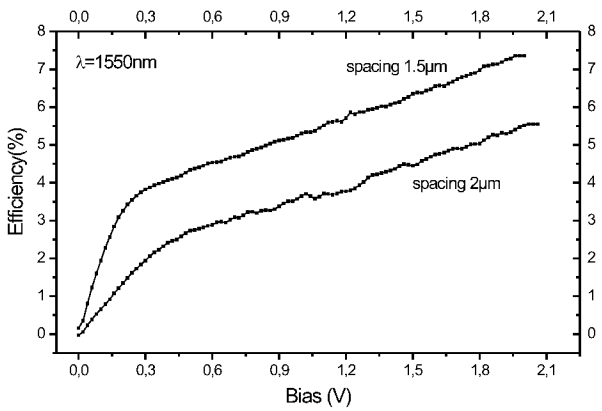

Figure 5.12: Total external quantum efficiency at $\lambda = 1550$ nm versus applied bias for a detector with an area of 100 μm^2 with 1.5 μm and 2 μm electrode spacing.

These overall efficiencies correspond to responsivities of 140 mA/W and 90 mA/W respectively. Considering the reflection losses at the germanium surface and that from the Cr electrodes (~50 % coverage), the calculated internal quantum efficiencies are 35 % for 1320 nm and 22 % for 1550 nm. Due to the linearity of the detectors in the low intensity regime, the quantum efficiency does not depend on the optical power intensity. However, the quantum efficiency decreases with increasing interelectrode distance (Fig. 5.12). This shows a higher carrier collection efficiency for a shorter drift carrier distance.

5.5.4 Electrical properties of the Ge film

The measured photocurrent data are well fitted by a simple two parameter model [47] based on the Hecht formula 5.4, adapted to a non-uniform field distribution (Fig 5.13). The adjusted parameters are the absorption coefficient, α, and mobility lifetime product, $\mu\tau$.

$$I_{ph} \approx q\alpha\Phi \cdot (\mu\tau)E \cdot \left[1 - e^{-d/(\mu\tau)E}\right] \tag{5.4}$$

where q is the elementary charge, α is the absorption coefficient, Φ is the photon flux, E is the electrical field, μ in the electron mobility and τ the carrier lifetime. Equation 5.4 is based on the rate equation and Ramos'

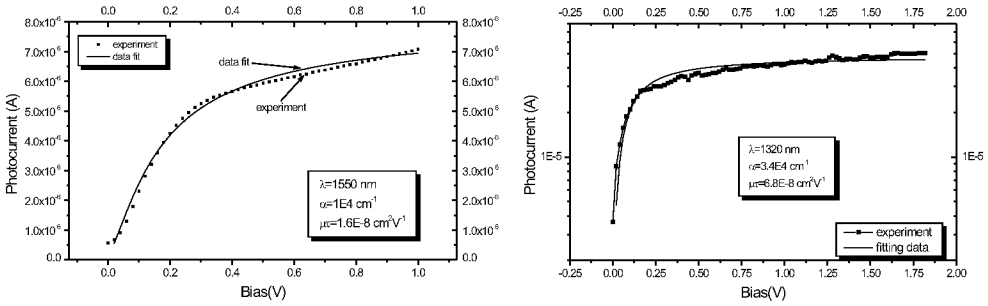

Figure 5.13: Photocurrent versus applied bias for a MGeM detector at 1320 nm and 1550 nm. The continuous line photocurrent fit with formula 5.4

theorem [45]. By solving the rate equation (5.5) at steady state conditions the distribution of excess carriers n(x,y) is obtained by:

$$\frac{dn(x,y)}{dt} = 0 = G + D_e\nabla^2 n + \mu_e E \cdot \nabla n - \frac{n}{\tau_e} + \mu_e n\frac{\rho}{\epsilon} \tag{5.5}$$

where G is the generation rate, D_e is the diffusion coefficient for electrons, ρ is the net charge density and ϵ is the dielectric constant. A carrier with the mobility μ moving in an electric field E generates a current given by Ramo's theorem:

$$I_e = \frac{q\mu_e E}{d} \tag{5.6}$$

and the total current is obtained by integrating the contributions of all electrons:

$$I_e = \frac{q}{d} \cdot \mu_e \cdot \int_0^H dz \int_0^w dy \int_0^d n(x,y,z)dx \tag{5.7}$$

where n(x,y,z)=n(x,y)$e^{-\alpha x}$ and H being the depth of the detectors. If N_0 is the number of electron-hole pairs generated in a detector at a distance x_0 from the negative contact, the total charge collected is:

$$Q(x_0) = \frac{qEN_0}{d} \cdot \left[(\mu\tau)_e \cdot (1 - e^{-\frac{d-x_0}{(\mu\tau)_e E}} + (\mu\tau)_h \cdot (1 - e^{-\frac{x_0}{(\mu\tau)_h E}} \right] \tag{5.8}$$

If the optical power is kept low to avoid space charge effects, the Hecht relation is obtain by replacing the electron-holes pairs with the number of absorbed photons per second [46]. Hence:

$$I(x_0) = \frac{qEP_{abs}}{dh\nu} \cdot \left[(\mu\tau)_e \cdot (1 - e^{-\frac{d-x_0}{(\mu\tau)_e E}} + (\mu\tau)_h \cdot (1 - e^{-\frac{x_0}{(\mu\tau)_h E}} \right] \tag{5.9}$$

where P_{abs} is the absorbed optical power and $h\nu$ is the photon energy. If, as is typical, $(\mu\tau)_e \gg (\mu\tau)_e$ the total charge collection is dominated by the electron contribution. From our data and from equation 5.4, an absorption coefficient of $\alpha = 1{\cdot}10^4$ cm^{-1} and a mobility life time product of $1.6{\cdot}10^{-8}$ cm^2V^{-1} were obtained at a wavelength of 1550 nm. For the wavelength of 1320 nm the absorption coefficient was determined to be α=$3.4{\cdot}10^4$ cm^{-1}. It is also observed that by increasing the electrode spacing from 2 μm to 3 μm the mobility lifetime product ($\mu\tau$) increases from $1.6{\cdot}10^{-8}$ cm^2V^{-1} to $6.8{\cdot}10^{-8}$ cm^2V^{-1}, which is equivalent to a shortening of the carrier's lifetime. It should be noted that a moving charge induces a current until it is collected at the electrode, or it recombines or it is trapped. Therefore the lifetime in equation 5.4 represents the mean recombination and trapping-detrapping time. The imperfections of the structure (misfits and/or threading dislocations) influence the lifetime of the carriers. A larger interelectrode spacing will be equivalent to a low collection probability for the carriers. This can be seen clearly by comparing the efficiencies measured at different electrode spacing (Fig. 5.12). It has been shown [36] that post growth annealing of the sample reduces the threading dislocation density and as a consequence, the mobility-lifetime product ($\mu\tau$) increases. In the table below a comparison of our data with the data from [36] is presented. The threading dislocation densities were measured in both cases by plan-view TEM. Mobility-lifetime products were estimated from measured photocurrent response of MSM photodetectors using the Hecht formula. No post growth annealing cycles were performed for our samples.

	Data from [36]		our detectors
Cyclic annealing temperature (°C)	NA	900/780	NA
Number of annealing cycles	0	20	0
Threading dislocation density (cm^{-2})	$9.5 \cdot 10^8$	$1.6 \cdot 10^7$	$1 \cdot 10^8$-10^8
Mobility-lifetime product (cm^2V^{-1})	$7 \cdot 10^8$	$3 \cdot 10^6$	1 $1 \cdot 10^8$-$7 \cdot 10^8$

5.6 Electrical time response measurements

The set-up used for measuring the response time of the detectors at an ultrashort optical excitation is described in the Chapter 3. The MSM interdigitated design has the advantage of low capacity (1-10 fF), which is reflected in a low RC time constant of the device (under 0.6 ps). For a 1 μm electrode spacing, the transit time for a carrier which is moving with saturation speed, is 8 ps. By comparing the transit time with the RC time constant, it can be concluded that time the response of the MGeM interdigitated devices depends on carrier dynamics only.

5.6.1 Optimum performance results

For studying the device response time, detectors with an active area of 100 μm^2 to 400 μm^2 were analyzed. No signal could be detected at 0 V bias, because the symmetrical structure does not provide a built-in potential. Fig. 5.14 shows the fastest response measured at wavelengths of 1300 nm and 1550 nm. The temporal response is essentially identical, while the electrical signal amplitude is higher at 1300 nm due to the higher quantum efficiency. The temporal response is a consequence of the carrier dynamics within the Ge film only. For an electrode spacing of 1.5 μm the carriers transit time is $\tau =$ 12.5 ps. The perfect agreement with the measured 12.5 ps FWHM response time demonstrates that carriers are moving with saturation drift velocity. The time for carriers to reach the saturation speed is about 60 fs. The pulse width, measured in the time domain, corresponds to a -3dB bandwidth of $f_{3dB} = \frac{1}{2\pi\tau_t} \sim$ 13 GHz. In contrast with the bulk MSM detector, in thin layer MSM detectors deep carrier creation is avoided, the absorption taking place only in the thin semiconductor layer [48]. Also, the detector active area being restricted to a region closer to the electrodes, a more uniform electrical field distribution in the active layer is obtained. Besides, modifications of

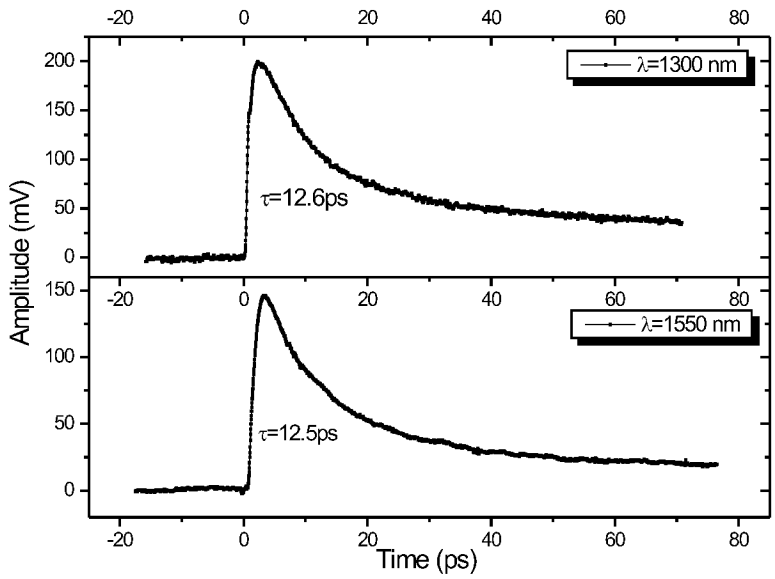

Figure 5.14: Electrical response from a MGeM detector with 1.5 μm electrode spacing at λ = 1300 nm (a) and 1550 nm (b). Applied bias voltage U = 4 V, optical power P_{opt} = 1 mW.

the electrical field distribution caused by the different dielectric constant of the Ge and Si may play a role. These different aspects contribute to the fact that thin film MSM detectors exhibit a faster response time than bulk MSM detectors [49]. The response time of 14 ps FWHM was reported in [35] from bulk Si MSM photodetectors with even a smaller (1.2 μm) electrode spacing. This data was obtained at an applied voltage of 12.5 V. In Ge the saturation speed is achieved at lower electrical field intensities, so low voltages are necessary to operate the detectors in the saturation regime. The response times presented in Fig. 5.14 are obtained at 4 V applied bias. In addition to avoiding the long particle path in low field regions, the speed of MGeM detectors with a thin top Ge over layer becomes independent of the light penetration depth, the effective absorption depth being limited to the Ge film.

5.6.2 Influence of the electrical field

The carrier acceleration within the Ge film is a function of the applied external field, which depends on the electrode spacing and the applied voltage. The carrier dynamics controls the pulse response. The pulse shape as a function of the applied voltage can be seen in Fig. 5.15. The excitation wavelength was 1550 nm. The signal was obtained from a detector with an area of 10 x 10 μm^2 and 1.5 μm electrode spacing. The shape of the pulse is characterized by the following features:

1. A very fast rise time.

2. A fast decay corresponding to the carrier sweep-out.

3. A subsequent slower tail

The rising part of the signal is due to the instantaneously induced current in the external circuit. This current stems from the charges moving inside the detector volume. It is limited by the carriers´effective mass, the attained speed and by an RC time constant, which includes the influence of the electrodes and the external coplanar lines. The decreasing part of the signal represents the rapid sweep-out of the carriers from the Ge layer. Due to the low capacitance of our photodetectors, the signal decay is not influenced by the RC time constant. As a consequence, the FWHM of the signal is primarily determined by the carrier dynamics. Its field dependence is a consequence of carrier acceleration. The total current j is the sum of the electron´ and hole´ contribution: $j = j_e + j_h$. In Ge electrons reach the saturation drift velocity vs at an electrical field $E = 3{\cdot}10^4$ V/cm and holes at E = $2{\cdot}10^4$ V/cm [11]. At an applied bias of 1 V ($E = 6{\cdot}10^3$ V/cm), the electrons move towards the anode, with saturation drift velocity and the holes attain a lower speed. The drift velocity of the holes increases with the field strength up to $E = 2{\cdot}10^4$ V/cm, until at 4 V ($E = 2.4{\cdot}10^4$ V/cm) the detector operates in the saturation regime, which gives the fastest response. Higher voltages are not advantageous anymore. The tail of the impulse response signal is ascribed to the trapping and detrapping processes. The interface between Si and Ge, where the mismatch induced stress is relieved, a significant amount of dislocations appear. These and other defects may act like carrier traps for the photo-generated charge carriers. If a large density of the traps is rather shallow, thermally activated hopping-transport is possible. Carrier escape from shallow traps is then expected to be responsible for the delayed current long after excitation.

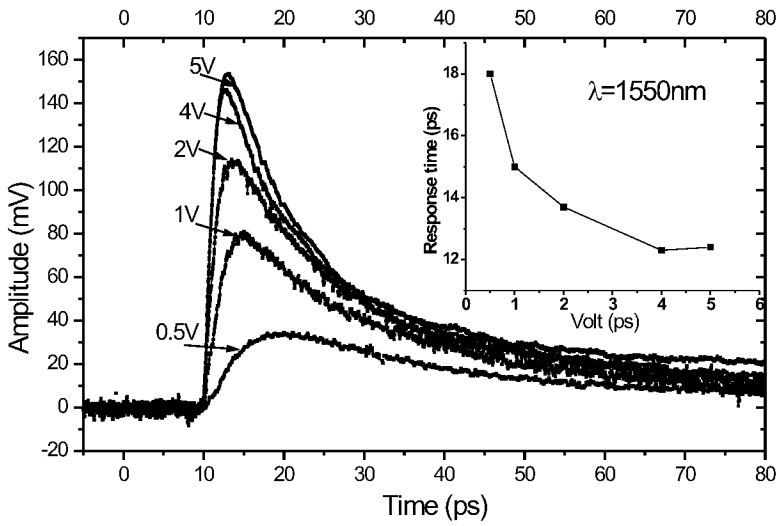

Figure 5.15: Electrical time response versus applied voltages from a MGeM detector with 1.5 μm electrode spacing. Optical power P_{opt} = 1 mW. The measured FWHM is shown in the inset.

5.6.3 Influence of the electrode spacing

The influence of the hole current on the total current can also be observed by changing the electrode separation at constant intensity and constant applied bias (the resulting electrical field is lower than that required for transport at saturation speed velocity of the holes). In Table 5.1, the measured response times are compared with calculated electron and hole drift time values for different electrode spacing detectors at an applied bias of 1V [11].

spacing (μm)	theoretical drift time for electrons (ps)	theoretical drift time for holes (ps)	measured FWHM (ps)
1.5	12.5	17.4	15.1
2	16.6	25	22.6
3	25.8	42.8	29.2

Table 5.1: Comparison of the calculated drift time and the measured FWHM for detectors with different spacing at an applied bias U = 1 V

As it is shown in Table 5.1, for a 3 μm electrode spacing, if the holes are

much slower than the electrons, the FWHM is governed by the electron pulse current. Theoretical calculations show that in this condition the electrons with a drift velocity of $5.8 \cdot 10^6$ cm/s will induce a current which terminates after 25.8 ps. The holes with a drift velocity of $3.5 \cdot 10^6$ cm/s will form a current pulse with duration of 42.8 ps. The measured FWHM of 29.2 ps shows that the detector response is governed by the electron current, the holes, being swept-out slowly, add their contribution to the tail of the response waveform. A continuous change of the pulse shape from mainly electron shape pulse to both electrons and holes pulses contribution is obtained by increasing the applied bias. The best performance of this detector with a FWHM of 25.2 ps is obtained at 7 V. The measured impulse responses from the detector with 3 μm spacing are presented in table 5.2.

Applied bias (V)	theoretical drift time for electrons (ps)	theoretical drift time for holes (ps)	measured FWHM (ps)
1	25.8	42.8	29.2
3	25	30	27.3
7	25	25	25.2

Table 5.2: Comparison of the calculated drift time and the measured FWHM for a detector with 3 μm spacing at different applied bias

5.6.4 Response to very high illumination power

Due to the submicrometer thickness of the Ge film and the correspondingly small sensitive Ge volume V$\simeq$100 μm^3, the detectors have a limited linearity range for high illumination powers. If the power of the incident light pulses is increased from 1 mW to 10 mW, a decrease of the response speed and a non-linear distortion of the pulse shape is observed, see Fig. 5.16. This figure shows the impulse response from a detector with 2 μm electrode spacing. At 1 mW power, an estimated density of 10^{17} e-h pairs/cm^3 is expected. At higher optical intensities the increasing carrier density leads to an increase in carrier recombination, a screening of the applied electrical field from the electrodes and a change in the reflectivity of the Ge film. This observation is based on a relatively small increase of the signal amplitude at an increasing ten times the excitation intensity. If the amount of space charges build-up after photoexcitation due to the spatial separation of electrons and holes, become large enough to cause an appreciable screening of the externally applied field strength which results in a delayed sweep-out of carriers. The shape of the pulse still has the general features of an initial rapid decay and

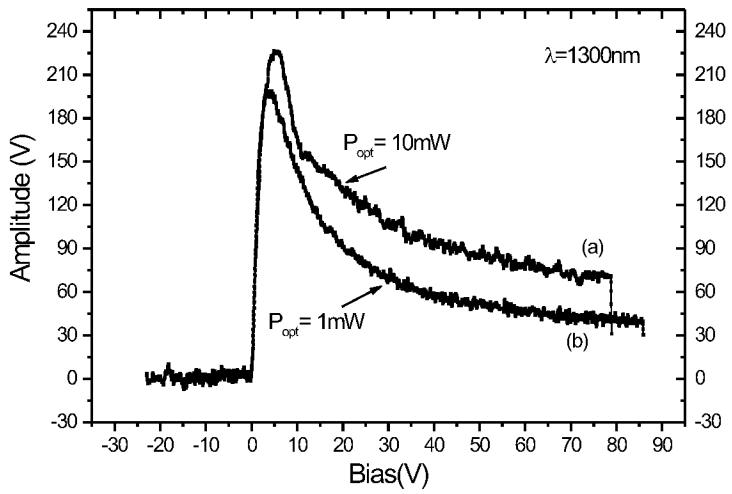

Figure 5.16: Electrical response from a MGeM detector with 2 μm electrode spacing at $\lambda = 1300$ nm for different incident optical power:(a) input optical power $P_{opt} = 10$ mW, (b)input optical power $P_{opt} = 1$ mW

a subsequent slow tail. The fast decay part originates from a decrease of the electron and hole current due to the screening rather than to a depletion of carriers. The long tail is in this case a contribution of both electrons and holes in equal measure. The presented results for high power (Fig. 5.16) are not a limitation for a possible applications, since these signal powers are far in excess of the typical powers used for actual applications.

5.6.5 Response to 800 nm wavelength signals

At a wavelength of 800 nm, the Si substrate acts as an additional detecting volume. This does not render the device useless, but a change of the response speed and the pulse shape is expected, see Fig. 5.17. In addition to the carriers created in the germanium layer, which are swept out quickly, additional carriers are collected from the Si substrate as well. This experiment clearly demonstrates that the thin active Ge layer improves the device speed. In this case an improvement of about 50 % is observed.

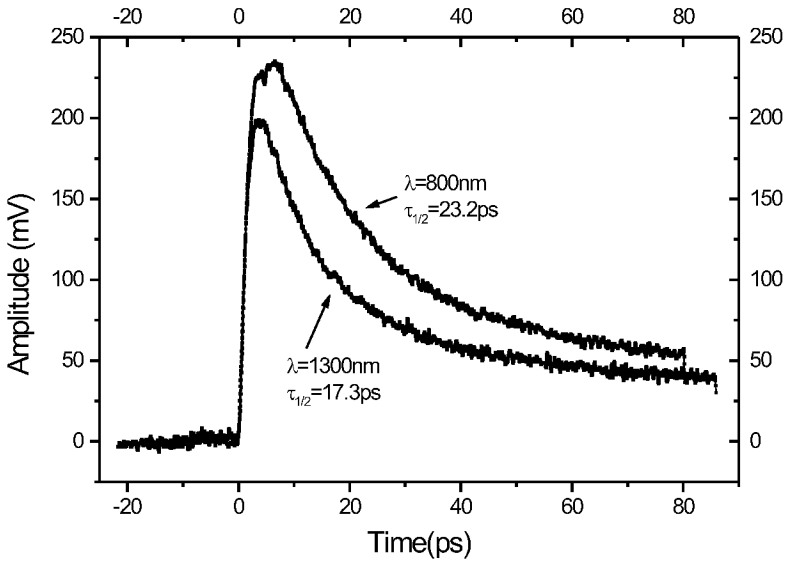

Figure 5.17: Electrical response from a MGeM detector with 2 μm electrode spacing at λ = 1300 nm and λ = 800 nm. Applied bias voltage U = 4V, optical power P_{opt} = 1 mW.

5.7 Conclusion

The high speed capability of MGSM photodetectors using a photosensitive epitaxial Ge film were demonstrated. Besides the direct bandgap transition at 0.86 eV, Ge has a few more advantages over Si: higher carrier mobility and lower electrical field intensity required for accelerating the carriers to saturation drift velocity. As compared to the undulating SiGe superlattice structures, the device fabrication processes would also be greatly simplified in the case of pure Ge detectors. These advantages give pure Ge detectors an edge over the former, for fast speed and low voltage device fabrication. For these reasons, it was intended to replace the SiGe layers with a pure Ge layer, maintaining the same detector design. The difficulties posed by lattice mismatch was overcome using a surfactant mediated epitaxy technique. By this method, an epitaxial Ge layer was grown on top of the $CoSi_2$ layer. Cross sectional TEM as well as RBS measurements once again demonstrated that these devices were of a high quality. The minimum yield obtained by ion channelling measurements were only 5%. Despite the good crystalline

quality of the specimens, the layer Schottky contacts could not be obtained due to the presence of high residual Sb concentration. High quality, low Sb concentration samples were obtained by MBE growth for 300 nm thick Ge layers directly on Si(111) without the intervening $CoSi_2$ layer. Planar interdigitated MSM design detectors were fabricated from these wafers. The interdigitated detectors have a low capacitance so that their response speed in limited only by the carriers transit time between electrodes. Using electron beam lithography, small inter-electrode distances could be realized for ultra-fast detectors. We have successfully shown in this chapter, that fast response speed can be obtained from thin film Ge detectors fabricated by completely standard optical lithography processes. Detectors with different interelectrode spacings were analyzed. Details of the temporal evolution of the response currents as a function of the applied voltage, electrode spacing, wavelength and the illumination intensity were analyzed and discussed. At low illumination intensities, a quantitative agreement between the experimental results and the theoretically expected carrier dynamics was found. For a finger spacing of 1.5 μm an electrical pulse width of 12.5 ps FWHM was measured for both wavelengths, 1300 nm and 1550 nm. The response time was equal to the calculated transit drift time. The usable bandwidth was found to exceed 10 GHz. An excessively high illumination intensity (10 mW) reduces the response time of the device. At high intensities, the detectors do not work in the linear regime anymore. This is however inconsequential for device applications, as such intensities are far in excess to what is practically used.

However, unlike the vertical MSM detectors there is no necessity to scale down the active area in order to avoid the RC limitation of the bandwidth. Due to its lower capacitance the interdigitated design permit the use of 4 times larger active area than vertical design. Moreover, waveguide detectors can be realized with substantially longer coupling length resulting in higher sensitivity devices.

Chapter 6

Conclusion

The central motivation of the present work is the development of ultra-fast Si based photodetectors for the IR range. Towards this end, two distinct types of devices were fabricated and their electric and electro-optic characteristics optimized.In order to determine the response speed of the detectors, a pump-probe technique with femtosecond light pulses was used. A new optical experiment was planned and build-up. Ultrashort optical pulses from a Ti:sapphire laser were coupled into an optical parametric oscillator. It was used to convert the Ti-sapphire pulses to the needed infrared wavelengths. The first type of photodetectors used $CoSi_2$ as one metal electrode and SiGe as the photosensitive semiconductor. In order to incorporate a sufficient amount of Ge, a new structure was used: the undulating layer superlattice is a way of forming a SiGe superlattice structure, which allows the growth of thicker layers and a higher germanium incorporation into the layers. Using this technique, novel photodetectors were designed and fabricated. The mesa structure ensures a homogeneous electric field across the light-absorbing layers and prevents carrier diffusion into low field region. The sensitivity of the device is enhanced by an optical cavity. Efficiencies of 5 % at 1320 nm and 0.9 % at 1550 nm were obtained. For the choice of the absorber thickness, a compromise between sensitivity and speed has to be found. Fast carrier sweep-out requires a thin layer between the contacts. For the device reported here, a record electrical time response of 9.4 ps at a wavelength of 1550 nm was measured. The detector response is limited by the RC time constant of the device. In order to obtain a sweep-out dominated speed, the lateral dimensions of the detector have to be minimized.
The second type of detectors used pure Ge as the photosensitive material. An epitaxial Ge film of 270 nm thickness was grown by surfactant mediated epitaxy on Si (111). If interdigitated top Cr electrodes were used as electrical contacts, good Schottky barriers were obtained. The speed of these detectors

is determined by the drift time of the photo-generated electrons and holes to the Cr fingers. For a finger spacing of 1.5 μm an electrical pulse width of 12.5 ps FWHM is measured for infrared radiation wavelengths of 1300 nm and 1550 nm, which is in agreement with the theoretically calculated value. Two advantages of using a thin Ge film are immediately seen: First, due to an effective absorption depth limited to the Ge film the speed of MGeM becomes independent of the light penetration depth. Second, a low applied bias is necessary to drive the detectors to the saturation regime (both electrons and holes having the saturation drift velocity). The overall quantum efficiency is 13 % at 1320 nm and drops to 7.5 % at 1550 nm. It has been shown that the quantum efficiency is constant for illumination intensities up to 1 mW. In summary, both detectors (vertical SiGe superlattice MSM detectors and planar interdigitated pure Ge detectors) show record response times for any silicon-based ultra-fast detectors at infrared wavelengths (1300 nm to 1550 nm) and hold substantial promise for future device applications.

Appendix A

Remarks on technological issues

A.1 The MBE system

Molecular beam epitaxy (MBE) was developed in the early 1970s as a means of growing high-purity epitaxial layers of compound semiconductors [50, 51]. Since that time it has evolved into a popular technique for growing III-V compound semiconductors as well as Si, Ge and several other materials. MBE can produce high-quality layers with very abrupt interfaces and good control of thickness, doping, and composition. Because of the high degree of control possible with MBE, it is a valuable tool in the development of sophisticated electronic and optoelectronic devices.

We used the MBE system for growth of semiconductor layers necessary for photodetectors fabrication. The heterostructures were grown in a MBE system with a base pressure of 2 x 10-11 mbar. Substrates with diameter up to 100 mm can be handled. The system is equipped with electron-beam evaporators for the materials Si, Ge and Co and effusion cells for the dopands Sb and B. The flux of the electron beam evaporators is controlled by optical sensors. The fluctuation of the fluxes over time is about 2 % for Si 5 % for Ge and 10 % for Co, the lateral homogenity of the deposition is 1 % for both Si, 9 % for Ge, 3 % for Co and 20 % for Sb. The MBE system is equipped with a quartz microbalance for thickness measurements, a mass spectrometer and a reflection high-energy electron diffraction (RHEED) system. The RHEED system is of great importance for the control of the processes for the Ge deposition on Si, because the RHEED pattern indicated the reconstruction of the surface. The RHEED patterns were monitored during growth interrupts. It was not possible to observe them during deposition because the stray fields of the electron-beam evaporators for Si and Ge strongly disturbed the electron beam of the RHEED system.

A.2 RCA cleaning procedure

Contaminants present on the surface of silicon wafers at the start of processing, or accumulated during processing, have to be removed at specific processing steps in order to obtain high performance and high reliability semiconductor devices, and to prevent contamination of process equipment, especially the high temperature oxidation, diffusion, and deposition tubes. The RCA clean is the industry standard for removing contaminants from wafers. Werner Kern developed the basic procedure in 1965 while working for RCA (Radio Corporation of America) - hence the name. The RCA cleaning procedure has three major steps used sequentially:

1. *Organic Clean*: Removal of insoluble organic contaminants with a 5:1:1 H_2O:H_2O_2:NH_4OH solution.
2. *Oxide Strip*: Removal of a thin silicon dioxide layer where metallic contaminants may accumulate as a result of (1), using a diluted 49:1 H_2O:HF solution.
3. *Ionic Clean*: Removal of ionic and heavy metal atomic contaminants using a solution of 6:1:1 H_2O:H_2O_2: HCl.

Procedure: The solution in a teflon beaker is placed into a temperature-controlled water bath and the power is adjust to maintain the solution at 80°C.The samples are placed on teflon carriers. The following steps are performed:

- Submerge the carrier with samples in the *Organic Clean* solution for 10 minutes.
- Remove samples' carrier from the solution bath and introduce it in the deionized (DI) water cascade.The samples are kept in the DI water until the water became high resistent ($\geq 10\Omega$·cm)
- Submerge the samples in the *Oxide Strip* solution for 30 seconds.
- Remove samples from the solution bath and introduce them in the deionized (DI) water cascade.
- Submerge samples in the *Ionic Clean* solution for 10 minutes.
- Remove samples from the bath and introduce them into the DI water beaker again.
- Remove carrier from the DI water beaker and blow dry with nitrogen.
- The samples are taken to next processing step or place in a carrier box.

A.3 Optical lithography

Photoresist is the general term for polymers that can create patterns by the use of solvents after irradiation. The development of the resist is based on a chemical reaction and depends on the solubility difference between irradiated and unirradiated areas.

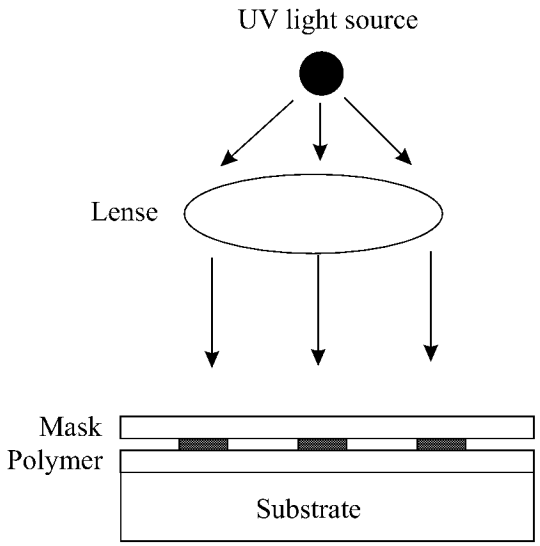

Figure A.1: Schematic presentation of optical lithography technique.

The optical lithography process parameters used for fabrication of the detectors presented in this work are summarized in Table A.1.

A.4 Reactive Ion Etching (RIE)

Devices are built from a number of different layers material deposited sequentially. The lithography process described in Appendix A.3 is used to replicate circuits and device features, and the desired pattern is transferred by etching methods. There are two main etching methods: Dry etching (which is synonymous with plasma assisted etching)and wet etching.
Dry etching technology is indispensable for fabricating three-dimensional building blocks for microelectronic applications. The fabrication technique demand etching processes with high etch rate and - selectivity, both for bulk - and surface micromachining. For the exact definition of the structures with high aspect ratios it is necessary that the anisotropy and surface texture can

Process	Parameter	Comments
Cleaning	Aceton,Propanol	
Backing	2 min Hotplate, 150 °C	surface drying
Adhesive: HMDS (Hexamethyldisilan)	4000 rpm,Dry 90 s at 90 °C on hotplate	adhesion increasing
Polymer 5214		
polymer spinning	4000 rpm , Dry 5 min at 90 °C on the Hotplate	thickness = 1400 nm
Corners removing	40 s exposure, 90 s developing in MIF326:H_2O 1:1	polymer non-uniformities removing
UV exposure	positive process: 3.6 s negative process:2.7 s	vacuumcontact
polymer backing	2 min at 115 °C	only for a negative process
blind exposure	17s	only for a negative process
developing	20 s MIF326:H_2O 1:1 (neg. process) 60 s MIF326:H_2O 1:1 (pos. process)	optic control of the proces
Polymer 5206		
polymer spinning	6000 rpm , Dry 2 min at 90 °C on Hotplate	thickness = 600 nm
Corners removing	40 s exposure, 90 s developing in MIF326:H_2O 1:1.25	polymer non-uniformities removing
UV exposure	positive process: 6 s negative process:2.4 s	vacuumcontact
polymer backing	2.30 min at 115 °C	only for a negative process
blind exposure	13s	only for a negative process
developing	17 s MIF326:H_2O 1:1.25 (neg. process) 60 s MIF326:H_2O 1:1.25 (pos. process)	optic control of the proces
polymer hardening	5 min at 150 °C	if a RIE etching will be performed

Table A.1: Parameters for optical lithography

be well controlled. By contrast, wet chemical etching results in isotropic etching, where both vertical and lateral etch rates are comparable. A plasma reactive ion etching (RIE)reactor is a parallel plate diode system in which the wafer is placed on an *rf* capacitive-coupled bottom electrode. The other electrode is bigger and grounded. The wafer is subject to a heavily bombardment of energetic ions from plasma as a result of a large negative self-bias at the wafer surface (Fig. A.2). Anisotropic etching is obtained because ion-enhanced chemical etching has a higher etching rate in the direction perpendicular to the wafer surface than in the parallel direction. The selectivity is obtained by choosing the proper etching gas.

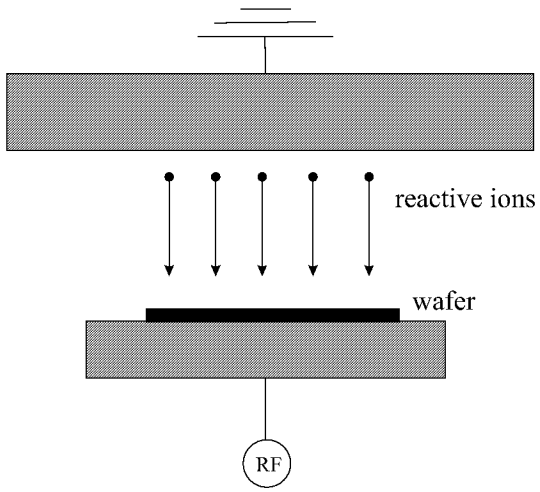

Figure A.2: Schematic of a diode type RIE reactor.

We used SF_6 gas for etching Si, Ge and SiGe materials. For opening windows in the silicon oxide layer CF_3 + CHF_3 gas was used. It provides a very good etch sensitivity of SiO_2 to Si. The process parameters for RIE of SiO_2 and Si are listed in Table A.2.

Material	Gas	Flux (cm^3s^{-1})	Pressure (Pa)	Rf-power (W)	DC-voltage (V)	Etch rate (nm /min)
SiO_2	CF_4 + CHF_3	20 / 20	3.0	300	700	40-50
SI	SF_6	20	2.5	100	280	30

Table A.2: Parameters for RIE of SiO_2 and Si.

List of Figures

List of Tables

Bibliography

[1] S.M.Sze, *Physics of semiconductor devices*, Second edition, Wiley, New York, (1981)

[2] E. H. Rhoderick *Metal-semiconductor contacts*, Cladendon, Oxford (1978)

[3] H. A. Bethe, *Theory of the boundary layer of crystal rectifiers*, MIT Radiat. Lab. Rep., Vol.43 (1942)

[4] G. Margaritondo, A. D. Katnani, H. G. Stoffel, R. R. Daniels, T. -X. Zhao, *Nature of band discontinuities at semiconductor heterojunction interfaces*, Solid State Commun., Vol.43, 163 (1982)

[5] C. G. van de Walle and R. Martin, *Theoretical study of Si/Ge interfaces*, J. Vac. Sci. Technol., Vol.B3, 1256 (1985)

[6] R. Strong, D. W. Greve, R. Misra, M. Weeks, P. Pellegrini, *GeSi infrared detectors*, Thin Solid Films, Vol.294, 343 (1997)

[7] R.People, *Physics and applications of* Ge_xSi_{1-x}/Si *straind-layer heterostructure*, IEEE Journal of Quantum Electronics, Vol.QE−22,No.9,1696 (1986).

[8] K. K. Choi, *The physics of quantum well infrared photodetectors*, World Scientific Publishing Co., 1997

[9] T. L. Lin, E. W. Jones, A. Ksendzov, S. M. Dejewski, R. W. Fathauer, T. N. Krabach, and J. Maserjian, *A novel Si-based LWIR detector: SiGe/Si heterojunction internal photoemission detector*, IEDM Digest Technical Papers, 641 (1990)

[10] Q. Wu and X. C. Zhang, *Free-space electro-optic sampling of terahertz beams* , Appl. Phys. Lett. 67, 3523 (1995).

[11] X. Yan et al., , Phys. Rev. Lett. 83, 3404 (2000).

[12] C.C. Davis, *Lasers and electro-optics: fundamentals and engineering*,Cambridge University Press, (1996).

[13] Bahaa E. A. Saleh, Malvin Carl Teich, *Fundamental of Photonics*, John Wiley and Sons Inc. (1991)

[14] www.coherent.com

[15] H. Lafontaine, N. L. Rowell,S.Janz, and D.-X. Xu, *Growth of undulating $Si_{0.5}Ge_{0.5}$ layers for photodetectors at λ=1.55 μm*, J.Appl.Phys.,Vol. 86 No.3, 1288 (1999).

[16] A. Splett, T. Zinke, K. Petermann, E. Kasper, H. Kibbe, H.-J. Herzog, and H. Presting, *Integration of waveguides and photodetectors in SiGe for 1.3 μm operation*, IEEE Photonics Technology Letters 6, 59 (1994).

[17] F. Y. Huang, X. Zhu, M. O. Tanner, and K. L. Wang, Appl. Phys. Lett. 67, 566 (1995).

[18] D. C. Houghton, D. D. Perovic, J.-M. Baribeau, and G. C. Weatherly, *Misfit strain relaxation in Ge_xSi_{1-x}/Si heterostructures: the structural stability of buried strained layers and strained-layer superlattices*, J. Appl. Phys. 67, 1850 (1990).

[19] Mool C. Gupta, *Handbook of Photonics*, CRC Press LLC (1997)

[20] D. D. Perovic, B. Bahierathan, H. Lafontaine, D. C. Houghton, and D.W. McComb, *Kinetic critical thickness for surface wave instability vs. misfit dislocation formation in Ge_xSi_{1-x}/Si (100) heterostructures*, Physica A 239, 11 (1997).

[21] H. Lafontaine, N. L. Rowell, and S. Janz, *Photon-resolved photoluminescence at λ=1.55 μm from $Si_{0.5}Ge_{0.5}$ epitaxial layers*, Appl. Phys. Lett. Vol.72, 2430 (1998).

[22] A. H. Van Ommen, C. W. T Bulle-Lieuwma, J. J. M. Ottenheim, and A. M. L. Theunissen, *Ion Beam Synthesis of heteroepitaxial $Si/CoSi_2/Si$ structures* J.Appl.Phys., Vol.67, No.4, 1767 (1990)

[23] S. Mantl *Molecular beam allotaxy: a new approach to epitaxial heterostructures*, J. Phys. D: Appl. Phys. Vol.31, 1 (1998)

[24] S. Mantl, R. Jebasinski and D. Hartmann, *The effect of dose on the growth of burried $CoSi_2$ layers in (111) and (100) Si produced by ion implantation*, Nuclear Instruments and Methods in Physics Research, B59/60, 666 (1991)

[25] J. M. Baribeau, *Interface morphology and relaxation in high temperature grown Si1-xGex/Si superlattices*, J. Cryst. Growth, Vol.157, 52 (1995).

[26] J. Tersoff, C. Teichert, M. G. Lagally, *Self-organization in growth of quantum dot superlattices*, Phys. Rev. Lett., Vol.76, 1675 (1996).

[27] Ch. Buchal, M. Löken, Th. Lipinsky, L. Kappius, and S. Mantl, *Ultrafast silicin based photodetectors*, J. Vac. Sci. Technol. A 18(2), 630 (2000).

[28] H. Zimmermann, *Integrated silicon optoelectronics*, Springer-Verlag, Berlin Heidelberg, 2000.

[29] R. People, J. C. Bean, D. V. Lang, A. M. Sergent, H. L. Stoermer, K .W. Wecht, R. T. Lynch and K. Baldwin, *Modulation dopping in* Ge_xSi_{1-x}/Si *strained-layer heterostructures* Appl.Phys.Lett. 45, 1231 (1984).

[30] D.-X. Xu, S. Janz, H. Lafontaine, and M. R. T. Pearson, *Photodetectors for 1.3 μm and 1.55 μm wavelengths using undulating MQWIs on SOI substrates*, Proc. SPIE, Vol.3630, 50 (1999).

[31] J. P. Hermanns, F. Rüders, E. Stein von Kamienski, H. G. Roskos, H. Kurz, O. Hollrichter, C. Buchal, and S. Mantl, *Vertical silicon metal-semiconductor-metal photodetectors with buried* $CiSi_2$ *contact*, Appl. Phys. Lett. Vol.66, No.7, 866 (1995).

[32] F.Rüders, J. Kim, M. Hacke, S. Mesters, Ch. Buchal and S. Mantl, *Vertical MSM photodiodes in silicon based on epitaxial* $Si/CoSi_2/Si$, Thin Solid Films, Vol.294, 352 (1997).

[33] C. Moglestue, J. Rosenzweig, J. Kuhl, M. Klingenstein, A. Axmann, Jo. Schneider, and A Hülsmann, *Picosecond pulse response characteristics of GaAs metal-semiconductor-metal photodetectors*, J. Appl. Phys. vol.70, No.4, 2435 (1991).

[34] J. B. D. Soole, H. Schumacher, *Transit-time limited frequency response of InGaAs MSM photodetectors*, IEEE Transactions on Electron Devices, Vol.37, 2285 (1990).

[35] S. Y. Chou and Y. Liu, *32 GHz metal-semiconductor-metal photodetectors on crystalline silicon*, Appl. Phys. Lett. Vol.61, No.15, 1760 (1992).

[36] L. Colace, G. Masini and G. Assanto, *Efficient high-speed near-infrared Ge photodetectors integrated on Si substrates* Appl. Phys. Lett. 76 (10), 1231 (2000).

[37] S. Mantl, L. Kappius, A. Antons, M. Löken, F. Klinghammer, M. Dolle, Q. T. Thao, S. Masters, Ch. Buchal, H. L. Bay, B. Kabius, H. Trinkhaus and K. H. Heing, *Growth, patterning and microelectronics applications of Epitaxial cobaltdisilicide*, Mater. Res. Soc. Symp. Proc., Advanced Interconnects and contact materials and processes for future IC, San Francisco, April 1998.

[38] M. Löken, L. Kappius, S. Mantl, and Ch. Buchal, *Fabrication of an Ultrafast Si Based MSM-Photodetectors*, Electronics Letters, Vol.34, 1027 (1998).

[39] L. Colace, G. Masini, F. Galluzzi and G. Assanto, *Metal-Ge-Si heterostructures for near-infrared light detection*, J. Vac. Sci. Technol. B, Vol.17, No.2, 465 (1999).

[40] D. Reinking, M. Kammler, M. Horn-von Hoegen, and K. R. Hofmann, *Enhanced Sb segregation in surfactant-mediated-heteroepitaxy: high-mobility, low-doped Ge on Si*, Appl. Phys. Lett., Vol.71, 924 (1997).

[41] D. J. Eaglesham and M. Cerullo, *Low-temperature growth of Ge on Si(100)*, Appl. Phys. Lett., Vol.58, 2276 (1991).

[42] M. Horn-von Hoegen, F. K. Le Goues, M. Copel, M. C. Reuter, and R. M. Tromp, *Defect self-annihilation in surfactant-mediated epitaxial growth*, Phys. Rev. Lett., Vol.67, 1130 (1991).

[43] S. Winnerl, L. Kappius, D. Buca, St. Lenk, Ch. Buchal, S. Mantl, *MBE-growth of a Ge-$CoSi_2$-Si heterostructure for vertical metal-semiconductor-metal photodetectors*, Microelectronic Engineering, Vol.60, 191 (2002).

[44] M. Horn-von Hoegen, J. Falta, M. Copel, and R. M. Tromp, *Surfactants in Si(111) homoepitaxy*, Appl. Phys. Lett., Vol.66, 487 (1995).

[45] S. Ramo, *Currents induces by electron motion*, Proc. I. R. E., Vol.27, 584 (1939).

[46] J. E. Toney, B. A. Brunett, T. E. Schlesinger, R. B. James, *Photocurrent mapping as a probe of transport properties and electric field distributions in cadmium zinc telluride detectors*, IEEE Transactions on Nuclear Science, Vol.44, No.4, 1684 (1997).

[47] L. Colace, G. Masini, F. Galluzzi, G. Assanto, G. Capellini, L. Di Gaspare, E. Palange, F. Evangelisti, *Near infrared light detectors based on*

UHV-CVD epitaxial Ge on Si(100), Materials and Devices for Silicon-Based Optoelectronics. Symposium, 193 (1998).

[48] Chia-Chi Wang; S.Alexandrou, D. Jacobs-Perkins,T. Y. Hsiang, *Comparison of the picosecond characteristics of silicon and silicon-on-sapphire metal-semiconductor-metal photodiodes*, Appl. Phys. Lett. Vol.64, No.26, 3578 (1994).

[49] M. Y. Liu, E. Chen, and S. Y. Chou, *140-GHz metal-semiconductor-metal photodetectors on silicon-on-insulator substrate with a scaled active layer*, Appl. Phys. Lett. Vol.65, No.7, 887 (1994).

[50] A. Cho, *Film Deposition by Molecular Beam Techniques*, J. Vac. Sci. Tech., Vol. 8, 31 (1971)

[51] A. Cho, J. Arthur, *Molecular Beam Epitaxy*, Prog. Solid-State Chem., Vol. 10, 157 (1975)

List of Publications

Publications in refereed journals

- *Metal-germanium-metal ultrafast infrared detectors*

  D. Buca, S. Winnerl, S. Lenk, S. Mantl and Ch. Buchal

  J. Appl. Phys., Vol. 92, 7599(2002).

- *Fast time response from Si/SiGe undulating layer superlattices*

  D. Buca, S. Winnerl, S. Lenk, Ch. Buchal, and D.-X. Xu

  Appl. Phys. Lett. 80, 4172 (2002).

- *Fast infrared-light detection in Si/SiGe superlattices with epitaxial buried $CoSi_2$ contacts*

  S. Winnerl, D. Buca, S. Lenk, Ch. Buchal and S. Mantl

  Microelectronic Engineering 64, 205 (2002).

- *MBE-growth of a $Si/CoSi_2/Ge$ heterostructure for vertical metal-semiconductor-metal photodetectors*

  S. Winnerl, L. Kappius, D. Buca, St. Lenk, Ch. Buchal and S. Mantl

  Microelectronic Engineering 60, 191 (2002).

- *MBE grown Si/SiGe undulating layer superlattices for infrared light detection*

  S. Winnerl, D. Buca, S. Lenk, Ch. Buchal, S. Mantl, and D.-X. Xu

  Materials Science & Engineering B 89, 73 (2002).

- *Femtosecond analysis of infrared MSM detectors*

  D. Buca, S. Winnerl, S. Mantl and Ch.Buchal

  Submitted to Physica E.

- *Low-temperature-grown MBE GaAs for terahertz photomixers*

  M. Mikulics, M. Marso, R. Adam, A. Fox, D. Buca, A. Forster, P. Kordos

  2001 International Symposium on Electron Devices for Microwave and Optoelectronic Applications. Proc. 9th EDMO, 155 (2001)

Contributions to conferences

- *Fast time response from Si-SiGe undulating layer superlattices*

  D. Buca, S. Winnerl, S. Lenk, Ch. Buchal

  Oral presentation at the Frühjahrstagung der DPG, Regensburg, 11-15 .03.2002.

- *Fabrication of vertical SiGe MSM photodetector for mid-IR radiation*

  D.Buca, St.Winnerl, Ch.Buchal, Dan-Xia Xu

  Poster presentation at the Frühjahrstagung der DPG, Hamburg, 2001.

- *Germanium MSM-Detektroren für Infrarotstrahlung*

  S. Winnerl, D. Buca, S. Lenk, Ch. Buchal and S. Mantl

  Oral presentation at the Frühjahrstagung der DPG, Regensburg, 11-15 .03.2002.2002.

- *Fast infrared-light detection in Si/SiGe superlattices with epitaxial burried $CoSi_2$ contacts*

  S. Winnerl, D. Buca, S. Lenk, Ch. Buchal and S. Mantl

  Poster presentation at the European Workshop Materials for Advanced Metallization Vaals, Niederlande, 2002 (will be published in Microelectronic Engineering).

  Performance optimisation of GaAs-based photomixers

  M. Mikulics, J. Darmo, D. Buca, A. Fox, , M. Marso, A. Forster, P. Kordos

  25^{th} Workshop on Compound Semiconductor Devices and Integrated Circuits, Cagliary-Italy, May 27-30, 2001

- *Gewellte Übergitter zur Infrarotdetektion*

  S. Winnerl, D. Buca, S. Lenk, Ch. Buchal, S. Mantl, and D.-X. Xu

  Oral presentation at the MBE-Workshop, Berlin, 2001.

- *MBE-Wachstum einer $Si/CoSi_2/Ge$ Heterostruktur für vertikale Photodetektoren*

  S. Winnerl, L. Kappius, S. Lenk, D. Buca, Ch. Buchal, und S. Mantl

  Oral presentation at the Frühjahrstagung der DPG, Hamburg, 2001.

Acknowledgments

Finally, I want to thank everybody who helped and supported me during this work. My special thanks go to:

Prof. Christoph Buchal
I consider it my good fortune to have had such a warm and engaging person as my thesis supervisor. I would first of all like to thank him for providing me the opportunity to carry out my research work at FZJ. Throughout the present work, he has shown tremendous patience, forbearance and unflagging enthusiasm. There is much that I have learnt from him through many hours of discussion. It is with gratitude that I shall always remember the unfailing concern and affection that he has shown towards me.

Prof. Siegfried Mantl
I would like to thank Prof. Mantl dearly for the interest he has expressed in my work. I have gleaned many fine insights from the discussions I have had with him. I deeply thank him for his support and encouragement.

Dr. Michael Löken
When I was still a "a babe in the woods", I found a mentor in M. Löken. He made me comfortable in my new environment and helped me in numerous ways. He introduced me to the various facilities and basically taught me the ropes. He is a good friend and I cannot thank him enough for all that he has done for me.

Dr. Stephan Winnerl
Through the years of my research work, I had the constant and warm friendship of Stephan Winnerl. There are times when even a full-grown man needs a shoulder to cry. I recall with fondness the many biking and in-line skating expeditions we had together. I would also like to thank him for introducing me to RBS and for the many useful technical hints that he gave me.

Dr. Daniel Lenssen
It is not often that one has an office mate who would be willing to answer a million questions a day and politely wait for the next one. With his excellent command over the German language, he helped me to translate numerous German texts. He was a treasure box of information and the answer to almost every question under the sun was only a mouse-click away for him.

Dr. Patrick Kluth and Qing-Tai Zhao
I would like to thank Qing-Tai and Patrick for giving me useful advise for operating the clean room facilities. They instructed in the fine art of etching and lithography. I would like to thank them for their help as well as their enthusiasm and friendship.

Dr. Susan Kluth - Hogg
It is not often that one is as much indebted to the wife as to the husband. While Patrick helped me to clean my samples, Suzy helped me to clean-up the written text. I thank her for patiently going through my papers and correcting grammatical errors.

Dipl. Phys. Adrian Petraru
My dear friend of many years and my fellow countryman has a an immense capacity for untangling knotty problems both in the real and theoretical world. He has more than willingly helped me with his tremendous skills. I would like to thank him for his warm friendship and support.

Dipl. Phys. Eduard Rije
I would like to thank Eduard for his immense capacity to take any amount of ribbing, his keen sense of humor and for his warm friendship.

Dipl. Phys. Martin Schmid and Opas Trithaveesak
My group mates for their friendship and for the good time we had together during conferences.

Frau Steffi Lenk
The high quality cross sectional TEM micrographs in my thesis were made possible because of the expertise of Steffi. Our friendship blossomed with the many flowering plants she generously gave to me. I would like to express my deep appreciation.

Frau Susanne Bippus
Our secretary, many thanks for her friendliness, efficiency and for ironing-out many administrative difficulties.

Mr.Andre Dahmen
The greatest misfortune that can befall a Ph.D aspirant is to have his computer fail on him at a crucial moment. I was fortunately saved from such a catastrophe because we had such a computer wizard in Andre.

Prof. Kordos und *Dipl. Phys. Martin Mikulics*
I like to thank Prof. Kordos and Martin Mikulics for the proposed collaboration and interesting experiments on GaAs and LT-GaAs materials.

Dipl.-Ing. A. Steffen and *Mr. Jürgen Müller*
They thankfully maintained the clean room facility in an immaculate condition. We are all very grateful for their support.

Special thanks go to *Mrs. Mona Nonn* for lithography mask fabrication and to *Mr. Josef Zillikens* for the metal deposition process.

Last, not least, my thanks go to my wife Lucia. She has with loving patience put-up with all my tantrums and seen to all my needs. She is indeed a tower of strength for me and without her encouragement, I would not have been able to concentrate on my work.

Forschungszentrum Jülich
in der Helmholtz-Gemeinschaft

Jül-4075
Juli 2003
ISSN 0944-2952